



Defense Threat Reduction Agency  
8725 John J. Kingman Road, Stop 6201  
Fort Belvoir, VA 22060-6201



DTRA-TR-05-15

**TECHNICAL REPORT**

# **Development and Testing of a Multiple Frequency Continuous Wave Radar for Target Detection and Classification**

Approved for public release; distribution is unlimited.

## **20070509266**

March 2007

N 00039-96-D-0051

Robert L. Rogers and  
Michael G. Anderson

Prepared by:  
University of Texas  
Applied Research Laboratories  
P. O. Box 8029  
Austin, TX 78713-8029

## **DESTRUCTION NOTICE**

**FOR CLASSIFIED** documents, follow the procedures in DoD 5550.22-M, National Industrial Security Program Operating Manual, Chapter 5, Section 7 (NISPOM) or DoD 5200.1-R, Information Security Program Regulation, Chapter 1X.

**FOR UNCLASSIFIED** limited documents, destroyed by any method that will prevent disclosure of contents or reconstruction of the document.

Retention of this document by DoD contractors is authorized in accordance with DoD 5220.22-M, Industrial Security Manual.

PLEASE NOTIFY THE DEFENSE THREAT REDUCTION AGENCY, ATTN: CST, 8725 JOHN J. KINGMAN ROAD, STOP-6201, FT BELVOIR, VA 22060-6201, IF YOUR ADDRESS IS INCORRECT, IF YOU WISH IT DELETED FROM THE DISTRIBUTION LIST, OR IF THE ADDRESSEE IS NO LONGER EMPLOYED BY YOUR ORGANIZATION.

# DISTRIBUTION LIST UPDATE

This mailer is provided to enable DTRA to maintain current distribution lists for reports. (We would appreciate you providing the requested information.)

- Add the individual listed to your distribution list.
- Delete the cited organization/individual.
- Change of address.

Note:  
Please return the mailing label from the document so that any additions, changes, corrections or deletions can be made easily. For distribution cancellation or more information call DTRA/CST (703) 767-4725.

NAME: \_\_\_\_\_

ORGANIZATION: \_\_\_\_\_

**OLD ADDRESS**

**NEW ADDRESS**

\_\_\_\_\_  
\_\_\_\_\_  
\_\_\_\_\_

\_\_\_\_\_  
\_\_\_\_\_  
\_\_\_\_\_

TELEPHONE NUMBER: (    ) \_\_\_\_\_

**DTRA PUBLICATION NUMBER/TITLE**

**CHANGES/DELETIONS/ADDITONS, etc.**  
*(Attach Sheet if more Space is Required)*

\_\_\_\_\_  
\_\_\_\_\_  
\_\_\_\_\_

\_\_\_\_\_  
\_\_\_\_\_  
\_\_\_\_\_

DTRA or other GOVERNMENT CONTRACT NUMBER: \_\_\_\_\_

CERTIFICATION of NEED-TO-KNOW BY GOVERNMENT SPONSOR (if other than DTRA):

SPONSORING ORGANIZATION: \_\_\_\_\_

CONTRACTING OFFICER or REPRESENTATIVE: \_\_\_\_\_

SIGNATURE: \_\_\_\_\_

DEFENSE THREAT REDUCTION AGENCY  
ATTN: CST  
8725 John J Kingman Road, MS 6201  
Fort Belvoir, VA 22060-6201

DEFENSE THREAT REDUCTION AGENCY  
ATTN:CST  
8725 John J Kingman Road, MS 6201  
Fort Belvoir, VA 22060-6201

# REPORT DOCUMENTATION PAGE

*Form Approved*  
OMB No. 0704-0188

Public reporting burden for this collection of information is estimated to average 1 hour per response, including the time for reviewing instructions, searching existing data sources, gathering and maintaining the data needed, and completing and reviewing this collection of information. Send comments regarding this burden estimate or any other aspect of this collection of information, including suggestions for reducing this burden to Department of Defense, Washington Headquarters Services, Directorate for Information Operations and Reports (0704-0188), 1215 Jefferson Davis Highway, Suite 1204, Arlington, VA 22202-4302. Respondents should be aware that notwithstanding any other provision of law, no person shall be subject to any penalty for failing to comply with a collection of information if it does not display a currently valid OMB control number. **PLEASE DO NOT RETURN YOUR FORM TO THE ABOVE ADDRESS.**

<b>1. REPORT DATE (DD-MM-YYYY)</b>	<b>2. REPORT TYPE</b> Technical	<b>3. DATES COVERED (From - To)</b> 28 July 2000 – 26 November 2004
------------------------------------	------------------------------------	--

<b>4. TITLE AND SUBTITLE</b>  Development and Testing of a Multiple Frequency Continuous Wave Radar for Target Detection and Classification	<b>5a. CONTRACT NUMBER</b> N 00039-96-D-0051
	<b>5b. GRANT NUMBER</b>
	<b>5c. PROGRAM ELEMENT NUMBER</b> 4695

<b>6. AUTHOR(S)</b>  Robert L. Rogers and Michael G. Andreson	<b>5d. PROJECT NUMBER</b> RG
	<b>5e. TASK NUMBER</b> RI
	<b>5f. WORK UNIT NUMBER</b> DH00001

<b>7. PERFORMING ORGANIZATION NAME(S) AND ADDRESS(ES)</b> University of Texas Applied Research Laboratories P. O. Box 8029 Austin, TX 78713-8029	<b>8. PERFORMING ORGANIZATION REPORT NUMBER</b>
--	---

<b>9. SPONSORING / MONITORING AGENCY NAME(S) AND ADDRESS(ES)</b> Defense Threat Reduction Agency 8725 John J. Kingman Road, MS 6201 Fort Belvoir, VA 22060-6201 CSNS/D. McDarby	<b>10. SPONSOR/MONITOR'S ACRONYM(S)</b> DTRA
	<b>11. SPONSOR/MONITOR'S REPORT NUMBER(S)</b> DTRA-TR-05-15

**12. DISTRIBUTION / AVAILABILITY STATEMENT**  
  
Approved for public release; distribution is unlimited.

**13. SUPPLEMENTARY NOTES**  
  
This work was sponsored by the Defense Threat Reduction Agency under RDT&E RMC code B 4695 C 3230 RG RI 00001 25904D.

**14. ABSTRACT**  
  
This report presents the development of a multiple frequency continuous wave radar for target detection and classification. The radar design incorporates specifications germane to both basic research and personnel detection applications. An extensive database of radar signatures is collected, processed, and analyzed. The radar signataure database contains data from human, vehicle and animal subjects. The subjects undergo significant variation in velocity, range, approach angle, and posture to represent potential operational conditions. The radar's detection and ranging performance is predicted and Tested. Classification performance is experimentally quantified using the acquired database.

**15. SUBJECT TERMS**

Multiple Frequency Continuous Wave	Doppler Radar Target Detection	Target Classification Radar Signatures
---------------------------------------	-----------------------------------	---

<b>16. SECURITY CLASSIFICATION OF:</b>			<b>17. LIMITATION OF ABSTRACT</b>	<b>18. NUMBER OF PAGES</b>	<b>19a. NAME OF RESPONSIBLE PERSON</b> Mr. David McDarby
<b>a. REPORT</b> UNCLASSIFIED	<b>b. ABSTRACT</b> UNCLASSIFIED	<b>c. THIS PAGE</b> UNCLASSIFIED			<b>19b. TELEPHONE NUMBER (include area code)</b> 703-767-4364

## Preface

This is the final report on work that Applied Research Laboratories, The University of Texas at Austin (ARL:UT), was tasked to perform under Cotntract N 00039-96-D-0051-3-21-1, Target Classifying Sensor.

# Table Of Contents

<b>Section</b>		<b>Page</b>
	Preface .....	ii
	Figures .....	vi
	Tables.....	viii
1	Introduction .....	1
	1.1 Motivation .....	1
	1.2 Objectives .....	1
	1.3 Organization of the Report .....	2
2	Joint Time-Frequency Signal Processing .....	4
	2.1 Motivation for Joint Time-Frequency Signal Processing.....	4
	2.2 Introduction to Joint Time-Frequency Processing.....	5
	2.3 The Short Time Fourier Transform .....	6
3	The Micro-Doppler Phenomenon.....	9
	3.1 Instantaneous Frequency .....	9
	3.2 Point Scatterer Model and Example Spectrogram.....	12
4	System Requirements and the MFCW Radar.....	14
	4.1 System Requirements .....	14
	4.2 Multiple Frequency Continuous Wave Radar Architecture .....	15
	4.3 MFCW Radar Target Range Calculation .....	18
5	Target Detection and Ranging.....	23
	5.1 Radar Range Equation .....	23
	5.2 Classical Detection Theory.....	24
	5.3 Detection in the Joint Time-Frequency Domain .....	29
	5.4 Procedure for Joint Time-Frequency Domain Detection .....	32
	5.5 Ranging in the Joint Time-Frequency Domain .....	35

## Table Of Contents (Continued)

Section	Page
6	Radar Hardware Design..... 39
6.1	Radar System Design..... 39
6.2	MFCW Radar Design ..... 40
6.3	System Design for Reduced Noise Figure..... 42
6.4	Analog to Digital Converter Limitations on Noise Floor ..... 44
7	Database Collection and Processing..... 46
7.1	Experimental Setup..... 46
7.2	Database Collection..... 47
7.3	Database Processing ..... 48
8	Results from Ranging, Detection, and Micro-Doppler Feature Evaluation ..... 51
8.1	Ranging Performance ..... 51
8.2	Detection Performance ..... 53
8.3	Spectrograms of Various Targets ..... 57
8.4	Radar Cost Analysis ..... 67
9	Theory and Design of Target Classification Systems ..... 69
9.1	Introduction ..... 69
9.2	Feature Extraction..... 70
9.3	Feature Space..... 74
9.4	Classifier Training and Testing ..... 75
9.5	Quantifying Classifier Performance with Confusion Matrices ..... 77
10	Classification Performance..... 81
10.1	Introduction ..... 81
10.2	Classifier Performance ..... 81
11	Conclusion ..... 88
11.1	Accomplishments and Future Work ..... 88

## Table Of Contents (Continued)

Section	Page
12    References .....	79
Appendix	
Glossary of Terms .....	A-1

## Figures

Figure		Page
1	Simulated time series (a) and DFT (b) of three-frequency waveform .....	4
2	Spectrogram of stepped-frequency waveform.....	6
3	Radar configuration .....	7
4	Constant velocity (a), constant acceleration (b), and constant jerk (c).....	9
5	Human point scatterer model with five scattering centers .....	10
6	Micro-Doppler features of a running human.....	11
7	MFCW radar block diagram.....	13
8	Quadrature demodulator .....	15
9	Three tone frequency separation.....	17
10	Probability density functions of noise and signal plus noise.....	21
11	Probability of detection versus SNR (a) and receiver operating curve (b).....	24
12	Complete spectrogram (a), extracted frame (b), and detected frame (c).....	29
13	Spectrogram frame for human target (a), detection results for threshold level -55dBm (b), -61dBm (c), and -76dBm (d) .....	30
14	Spectrogram (a) and TFR gram (b) of human jogging from 292 ft to 15 ft .....	32
15	Centroid frequency (a) and target range (b) .....	33
16	Receiver front end with two LNAs before the power dividers.....	37
17	Urban testing environment .....	40
18	Mobile data collection platform (a) and close-up view (b) .....	41

## Figures (Continued)

Figure		Page
19	3 FCW radar processing prior to joint time-frequency detection.....	42
20	Magnitude of fourth-order elliptic high-pass filter transfer function .....	43
21	Spectrogram with strong image target (a) and corrected spectrogram (b) .....	44
22	Spectrogram (a) and TFR gram (b) of corner reflector at 200 ft.....	45
23	Corner reflector range results at 200 ft with $\Delta f = 1$ MHz (b) .....	46
24	Range results for a human jogging from 292 ft to 15 ft with $\Delta f = 1$ MHz (a) and 16 MHz (b).....	47
25	Spectrogram of jogging human before (a) and after (b) detection .....	49
26	Number of detections per FFT (a) and received power (b) for jogging human .....	50
27	Spectrogram of human running (a), jogging (c), and walking (d). Expanded views are (b), (d), and (f), respectively.....	51
28	Human target walking at $45^\circ$ (a) and $90^\circ$ (b) relative to radar.....	52
29	Human crawling (a) transition from walking to crawling (b) .....	53
30	Vehicle driving at different velocities and accelerations.....	54
31	Vehicle driving at $45^\circ$ (a) and $90^\circ$ (b) relative to radar .....	55
32	Vehicle turning in front of radar at close range.....	55
33	Micro-Doppler produced by engine is visible at close range .....	56
34	Spectrogram of dog (a), goat (c), and deer (d). Expanded views are (b), (d) and (f), respectively .....	57
35	Multiple targets moving in opposite directions (a) and the same direction (b).....	58

## Figures (Continued)

Figure		Page
36	Spectrogram of ambient conditions (a) and human target (b) during heavy rain.....	59
37	Block diagram of a typical real-time classification system.....	61
38	Instantaneous bandwidth .....	63
39	Calculating legswing period: spectrogram (a), $x[n]$ (b), and auto-covariance (c) .....	65
40	Two-dimensional view of feature space (testing set).....	66
41	Offline training sequence.....	67
42	Office testing sequence.....	67

## Tables

Table		Page
1	Sensor system requirements .....	12
2	Ranging parameters .....	19
3	Detection parameters .....	28
4	Factors influencing design parameter selection.....	35
5	Front-end component noise figures and gains.....	37
6	Varying receiver specifications by changing number and position of LNAs.....	38
7	Empirical range accuracy results.....	46
8	Maximum detectable target ranges for $P_d = 0.9$ and $P_{fa} = 3.3 \times 10^{-7}$ .....	48
9	Empirical maximum detectable range .....	50
10	Small quantity radar cost analysis .....	60
11	Two-class confusion matrix.....	68
12	Three-class confusion matrix.....	69
13	Modified three-class confusion matrix.....	71
14	three-class confusion matrix of combined database .....	72
15	Two-class confusion matrix of combined database.....	73
16	Two-class confusion matrix with only goats in the animal class .....	74
17	Two-class matrix with only dogs in the animal class.....	74
18	Two-class confusion matrix with only deer in the animal class.....	75
19	Three-class confusion matrix with only crawlers in the human class .....	75

## Tables (Continued)

Table		Page
20	Two-class confusion matrix with only crawlers in the human subset.....	76
21	Three-class confusion matrix with only multiple-target files in the human and vehicle classes.....	77
22	Two-class confusion matrix with only multiple-target files in the threat class.....	77

# Section 1

## Introduction

### 1.1 Motivation.

Micro-Doppler refers to Doppler scattering returns produced by non rigid-body motion. Micro-Doppler gives rise to many detailed radar image features in addition to those associated with bulk target motion. Targets of different classes often create micro-Doppler images readily distinguishable even by untrained observers. Micro-Doppler features can be implemented in new target classification algorithms or used to enhance existing algorithms. The target classification potential of micro-Doppler attracts researchers in both the personnel detection and basic research communities. The basic research community also uses micro-Doppler to study the complex scattering from dynamic targets.

### 1.2 Objectives.

The goals for this project are mainly influenced by the needs of both the personnel detection and basic research communities. The main objective is to collect and process an extensive radar signature database to study micro-Doppler and design a robust classification algorithm. To accomplish this objective, radar hardware must be designed and built that is capable of acquiring high resolution micro-Doppler signatures. The radar hardware should be relatively low cost and have the ability to detect and process targets at useful ranges to interest the personnel detection community. The micro-Doppler signature database should be as large and diverse as possible, including a variety of signatures from different target types. In summary, the primary goals are to design hardware, develop signal processing algorithms, and collect a database to support micro-Doppler and target classification research.

### 1.3 Organization of the Report.

Section 2 introduces the main concepts of joint time-frequency processing. The Short-Time Fourier transform (STFT) is discussed since it is used extensively throughout the Report. Section 3 serves as an introduction to the micro-Doppler phenomenon. Both theoretical and empirical micro-Doppler signatures are included in this chapter.

The radar design begins in Section 4 with a discussion of system specifications and potential hardware architectures. An investigation of the Multiple Frequency Continuous Wave (MFCW) radar architecture follows the design specifications.

Section 4 concludes with the theory of target ranging using MFCW radars. Section 5 develops the theory of target detection and ranging. First, important results from classical detection theory are thoroughly reviewed. The following section covers joint time-frequency detection. The remaining sections involve specific procedures for target detection and ranging in the joint time-frequency domain, including an introduction to the Time Frequency Range Diagram (TFRgram).

The design of MFCW radar hardware to meet system specifications is covered in Section 6. The discussion is focused on receiver front-end noise figure reduction. Section 7 begins with an overview of the data collection setup. The chapter then details the contents of the collected radar signature database. Section 7 ends with a discussion of signal processing prior to joint time-frequency detection.

The results of radar ranging and detection testing and database processing are contained in Section 8. The first two sections cover ranging and detection performance. A wide variety of micro-Doppler signatures are displayed and analyzed in Section 8. The section also includes an analysis of system cost.

Section 9 presents aspects of target classification theory relevant to this work. Feature extraction and refinement, feature space, and confusion matrices comprise most of the theoretical discussion. Section 9 also includes a discussion of the classification features, training method, and testing algorithm used for this project.

Target classification results are presented and evaluated in Section 10. Section 11 concludes the report with an overview of system performance and a discussion of potential system improvements.

## Section 2

### Joint Time-Frequency Signal Processing

#### 2.1 Motivation for Joint Time-Frequency Processing.

This section reviews important concepts from joint time-frequency processing of baseband signals. Consider the complex signal  $x_{bb}(t) = i(t) + jq(t)$  where  $i(t)$  is the received signal in-phase component and  $q(t)$  is the quadrature component. The signal  $x_{bb}(t)$  is an (approximately) band-limited continuous-time waveform modulated in both amplitude and phase. An analog to digital converter samples the baseband signal at the rate of  $F_s$  Hz. Thus, the digitized waveform is

$$x[n] = x_{bb}(nT_s) \quad T_s = 1/F_s. \quad (1)$$

where  $T_s$  is the sampling period and  $n$  is an integer discrete time index. For stationary signals, the Discrete Fourier Transform (DFT) is employed to analyze spectral content. The DFT of a discrete time signal  $x[n]$  is defined as

$$X[k] = \sum_{n=0}^{N-1} x[n] e^{-j2\pi nk/N}, \quad k = 0, 1, \dots, N-1 \quad (2)$$

where  $k$  is the discrete frequency index and  $N$  is the length of the DFT. Similarly, the Inverse Discrete Fourier Transform (IDFT) is defined as

$$x[n] = \frac{1}{N} \sum_{k=0}^{N-1} X[k] e^{j2\pi nk/N}, \quad n = 0, 1, \dots, N-1 \quad (3)$$

Figure 1(a) on the next page shows the real part of a simulated stepped-frequency waveform that goes through three frequency steps: 200Hz, 400Hz, and then -100Hz. The results after computing the DFT of this signal are shown in Figure 2.1(b).

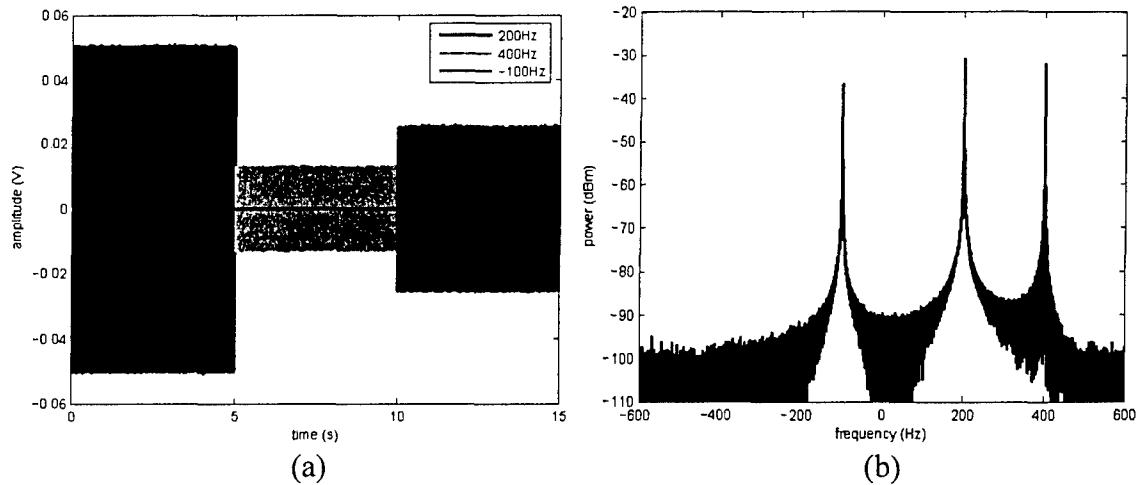


Figure 1. Simulated time series (a) and DFT (b) of three-frequency waveform.

The DFT reveals signal energy at the correct frequencies of 200Hz, 400Hz, and -100Hz. However, all information on *when* a certain frequency occurred within the signal is lost in this display. We would like to know that the signal of Figure 1(a) was 200 Hz from 0 to 5 seconds, 400 Hz from 5 to 10 seconds, and -100 Hz from 10 to 15 seconds. Similarly, Doppler radar signal processing seeks to estimate the frequency, strength, and time-location of multi-component received signals. Due to the non-stationary (time-varying statistics) nature of radar waveforms, the DFT alone is unsuitable for Doppler processing.

## 2.2 Introduction to Joint Time-Frequency Processing.

Joint Time-Frequency (JTF) techniques have recently received considerable attention in the signal processing literature due to their ability to process non-stationary signals [1], [2]. Most time-frequency transforms fall into either the linear or quadratic classification. Some well known linear time-frequency transforms are the Short-Time Fourier Transform (STFT) and the Continuous Wavelet Transform (CWT). The Wigner-Ville Distribution (WVD) and the Time-Frequency Distribution Series (TFDS) are two common examples of quadratic time-frequency transforms.

In this work, we use the Short-Time Fourier Transform (STFT) for joint time-frequency processing. The STFT was chosen despite its two primary drawbacks. The first drawback is the time-frequency resolution limit imposed by the STFT window function (to be discussed). Another disadvantage of the STFT is that it does not fully satisfy the mathematical properties of a time-frequency distribution. However, the STFT also has many advantages such as fast execution and intuitive interpretation that justify its use.

### 2.3 The Short Time Fourier Transform.

The discrete short-time Fourier transform of a signal  $x[n]$  is defined as

$$STFT_x[k, n] = \sum_{r=-\infty}^{\infty} x[r]w[n-r]e^{-j2\pi rk/N}, \quad k = 0, 1, \dots, N-1 \quad (4)$$

where  $n$  is the discrete time index,  $k$  is the discrete frequency index, and  $w$  is a window function. The STFT can be viewed as the Fourier transform of a signal multiplied by a window function that slides in time. The duration of the window is typically chosen such that the signal of interest is approximately stationary over the duration of the window. A shorter duration window provides better time resolution at the cost of reduced frequency resolution. Similarly, a longer duration window offers better frequency resolution at the cost of degraded time resolution. This is the well-known time-frequency resolution tradeoff inherent in the STFT.  $w[n]$

In order to extract useful signal parameters such as instantaneous frequency or bandwidth, we introduce the spectrogram. The spectrogram of  $x[n]$  is defined as the magnitude-squared of the STFT

$$Spectrogram_x[k, n] \triangleq |STFT_x[k, n]|^2 \quad (5)$$

Two important features of the spectrogram are that its values are (by definition) both real and nonnegative. To be classified as a time-frequency *distribution*, a function of time and frequency must be everywhere nonnegative and satisfy the corresponding marginals [1]. The time and frequency marginals are, respectively

$$\sum_k Spectrogram_x[k, n] = |x[n]|^2 \quad (6)$$

$$\sum_n Spectrogram_x[k, n] = |X[k]|^2 \quad (7)$$

One of the primary disadvantages of the spectrogram is that it does *not* satisfy the time and frequency marginals. The impact of this disadvantage shows up when attempting to estimate a signal's instantaneous frequency. Despite the fact that the spectrogram is not a true time-frequency distribution, it is still quite useful in radar signal processing. Figure 2 below shows a spectrogram image of the stepped-frequency waveform in Figure 1(a).

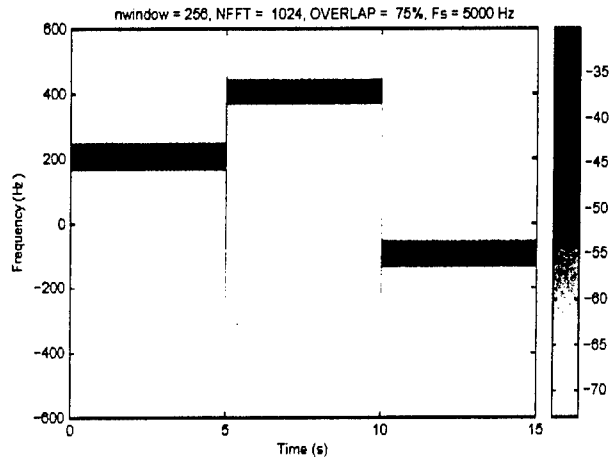


Figure 2. Spectrogram of stepped-frequency waveform.

The sample rate of the original time-domain waveform was 5 kHz, and the spectrogram window duration is 256 points. The type of window used was the Kaiser window with beta equal to 7 and the size of each FFT was 1024 points. These are typical values used for the spectrograms in this report. Along the horizontal axis is time in seconds while frequency in Hertz is along the vertical axis. The grayscale color shows the power (in dBm) of each signal component. As expected, the spectrogram reveals a 200 Hz signal from 0 seconds to 5 seconds, followed by a 400 Hz signal from 5 seconds to 10 seconds, and finally a -100 Hz component.

## Section 3 The Micro-Doppler Phenomenon

### 3.1 Instantaneous Frequency.

Consider the scenario of Figure 3 below. A transmitted radar pulse of frequency  $s_{TX}(t) = f_c$  travels a distance  $R(t)$  to a target. The target scatters the pulse and the receiver processes a signal that is proportional to the time-delayed transmit pulse.  $s_{RX}(t)$

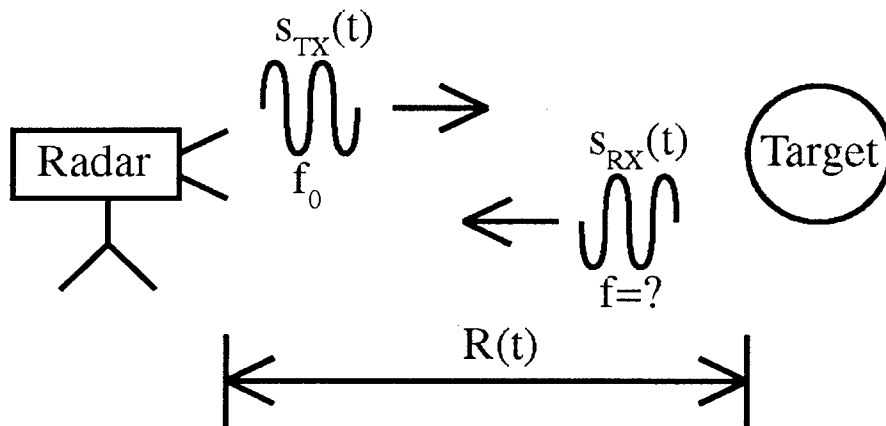


Figure 3. Radar configuration.

For a single target moving relative to the radar, the round-trip time delay  $\tau(t)$  becomes

$$\tau(t) = \frac{\text{distance traveled}}{\text{speed}} = \frac{2R(t)}{c} \quad (8)$$

where  $c$  is the speed of electromagnetic waves in the transmission medium and

$$R(t) = R_0 - v_R t - \frac{1}{2} a_R t^2 - \frac{1}{3} j_R t^3 + \text{higher order terms} \quad (9)$$

Here  $R_0$ ,  $v_R$ ,  $a_R$ , and  $j_R$  are the position, velocity, acceleration, and jerk of the target relative to the radar (at the time of demodulation).

The signal present at the receiver input is

$$\begin{aligned}
s_{RX}(t) &= \Gamma(t) \exp\{j[2\pi f_0(t - \tau(t)) + \psi_0]\} \\
&= \Gamma(t) \exp\{j[2\pi f_0 t - \frac{4\pi f_0 R(t)}{c} + \psi_0]\} \\
&= \Gamma(t) \exp\{j\Phi(t)\}
\end{aligned} \tag{10}$$

where  $\psi_0$  is a constant phase offset at time  $t$ ,  $\Gamma(t)$  is the received signal amplitude, and  $\Phi(t)$  is the phase. The instantaneous frequency of the received signal is proportional to the time derivative of the phase  $\Phi(t)$ :

$$f_{inst}(t) = \frac{1}{2\pi} \frac{d\Phi(t)}{dt} = f_0 - \frac{2f_0}{c} \frac{dR(t)}{dt} = f_0 + \frac{2f_0 v_R}{c} + \frac{2f_0 a_R t}{c} + \frac{2f_0 j_R t^2}{c} \tag{11}$$

where we have neglected the higher order terms. The first term is the radar transmit frequency and the second term we recognize as the classical Doppler frequency. The third term results in linear frequency variation over time, while the fourth term results in quadratic frequency variation over time.

In a fully coherent radar system, the Doppler frequency is extracted by mixing the receive signal with both an in-phase and a quadrature local oscillator of frequency  $f_0$ . Thus, the sign of the Doppler frequency is preserved which distinguishes approaching from receding targets. The instantaneous frequency of the baseband signal is then

$$f_{bb}(t) = \frac{2f_0 v_R}{c} + \frac{2f_0 a_R t}{c} + \frac{2f_0 j_R t^2}{c} \tag{12}$$

Figure 4 on the next page illustrates the effect of various simulated target motions. The SNR in each spectrogram is 15dB and the noise floor is -74 dBm.

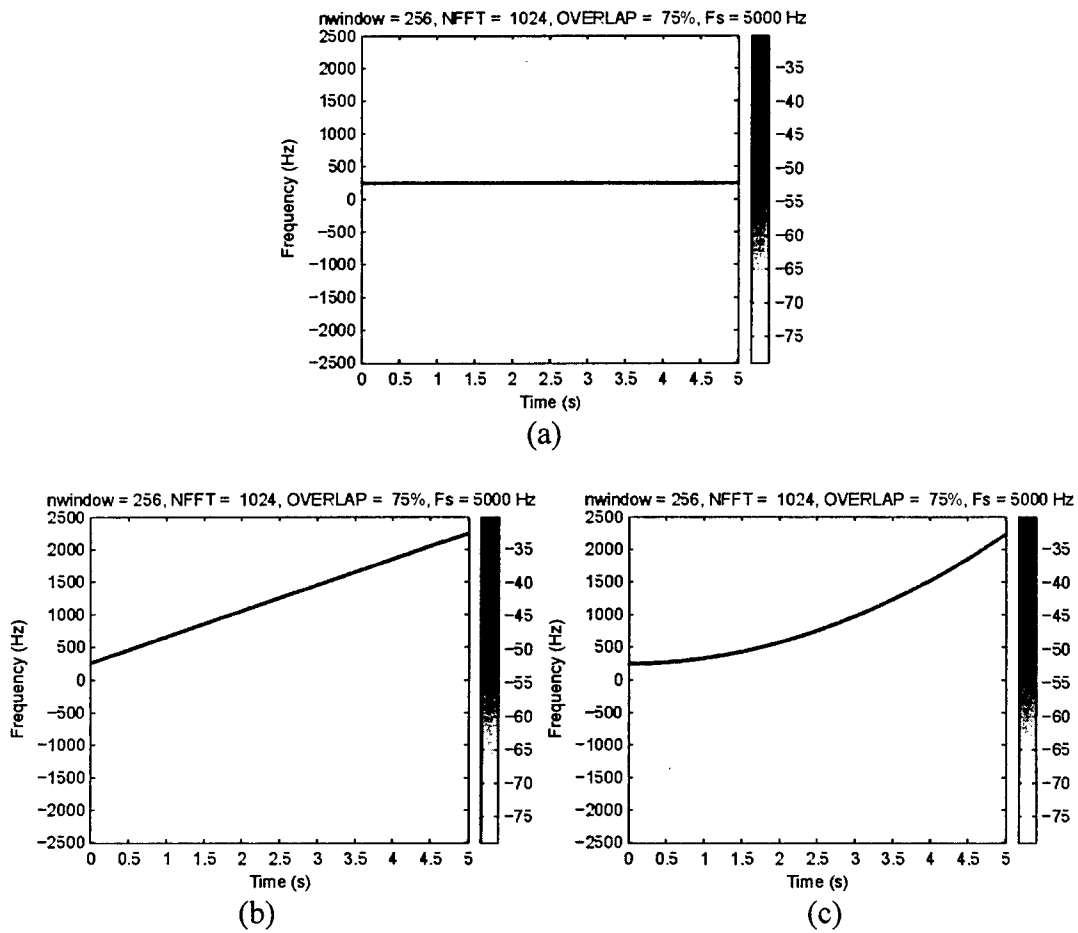


Figure 4. Constant velocity (a), constant acceleration (b), and constant jerk (c).

In Figure 4(a), a simulated target approaches the radar at 3.72 m/s (8.32 mph). This constant velocity results in a constant instantaneous frequency of 250 Hz. Figure 4(b) shows a target approaching the radar with a constant acceleration of  $6.0 \text{ m/s}^2$ . Hence, quadratic phase terms result in linear instantaneous frequency terms. In Figure 4(c), a target approaches the radar with a constant jerk of  $1.2 \text{ m/s}^3$ . As expected, cubic phase terms produce quadratic instantaneous frequency terms. These results will be crucial in interpreting the spectrograms of complex targets.

### 3.2 Point Scatterer Model and Example Spectrogram.

In order to gain intuition on the spectrograms of advanced targets, we use the point scatterer model. The point scatterer model is a widely used electromagnetic signal model.

In essence, the point scatterer model takes a target with a continuum of scattering sites and reduces them to a small number of point scattering centers. Figure 5 below illustrates a human walking toward a radar.

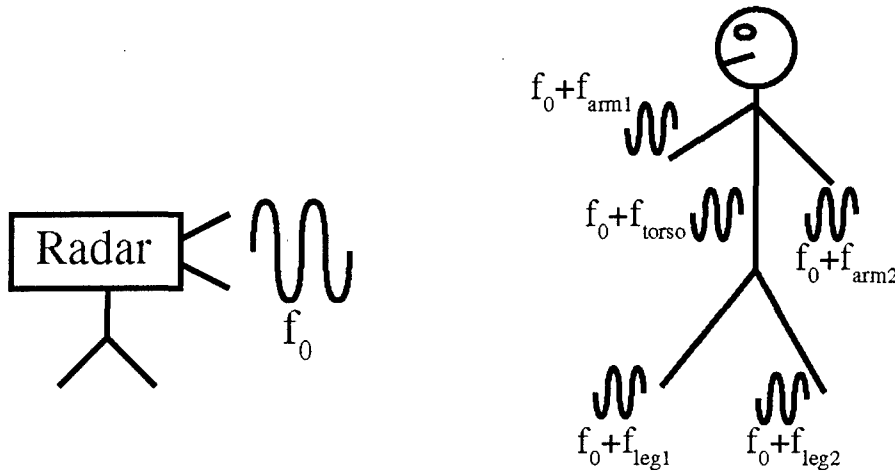


Figure 5. Human point scatterer model with five scattering centers.

One possible point scatterer model would consolidate the scattering from a human target into five scattering centers. One scattering center would correspond to the returns from the torso, and each arm and leg would have its own scattering center. Every point scatterer in this model articulates with its own velocity, and thus we associate individual Doppler frequency returns for each point scatterer. All Doppler returns not originating from the torso (non rigid-body motion) are defined as *micro-Doppler*. Adding more scattering centers would result in a more accurate target representation [3], but the five scattering center model for a human is a good tradeoff between accuracy, complexity, and intuition.

Figure 6 below displays actual radar data of a human running toward the radar.

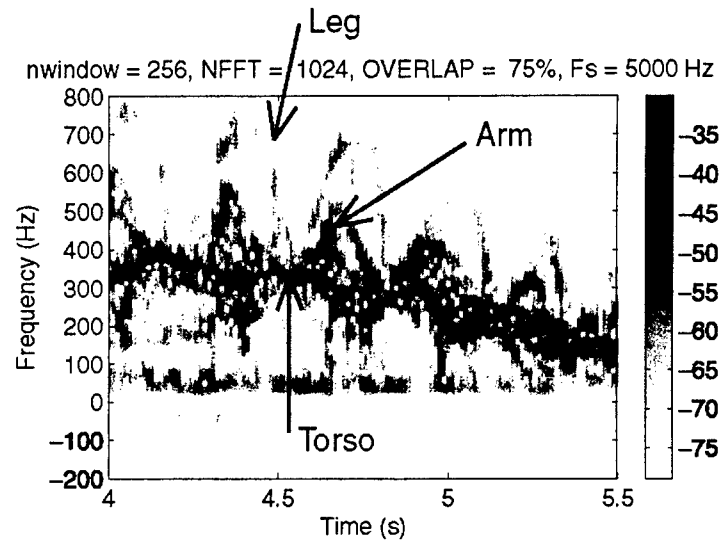


Figure 6. Micro-Doppler features of a running human.

The strong, approximately linear return near the center of the spectrogram is due to the torso. The large looping returns come from leg motion. The smaller returns closer to the torso are from the arms. We see in Figure 6 that actual human radar data can be described quite well with a five scattering centers approximation. We will discuss this further in Section 8.

## Section 4

### System Requirements and the MFCW Radar

#### 4.1 System Requirements.

A primary goal for this project was to build a relatively low cost radar that can produce high-resolution micro-Doppler signatures for target classification. The two major application areas for this research are personnel detection and basic research. The personnel detection community would be interested in exploiting micro-Doppler features for target classifying systems. Investigation of the complex electromagnetic scattering that gives rise to various micro-Doppler features is of interest to the basic research community. The system specifications for this project address the needs of both basic research and personnel detection applications. Table 1 below lists the sensor system requirements.

Table 1. Sensor system requirements.

Requirement Name	Value
90% detection range for all TOI	65 m (213 ft)
Average system false alarm rate	7 days
Range accuracy (90% detection)	1 m (3.28 ft)
Maximum unambiguous range	125 m (410 ft)
Azimuth angular coverage	20°, minimum
Per-unit production cost	less than \$1000

The first requirement is the detection range for all Targets Of Interest (TOI) given a 90% probability of detection and a fixed probability of false alarm. This probability of false alarm is set by the minimum acceptable average system false alarm time. The range accuracy specification of 1m is fairly coarse relative to the expected target dimensions. However, it is expected that range accuracies of this order will be sufficient for use in target recognition algorithms while not significantly increasing system costs. The specified minimum azimuth angular coverage is 20°. Several sensors (or a single sensor with wider azimuth beamwidth antennas) could be used to provide wider coverage areas in personnel detection applications. The target system per-unit cost is under \$1,000.

Several radar architectures were investigated to potentially meet these system specifications. The goal to study micro-Doppler narrowed the scope to Continuous Wave (CW) radars that provide good Doppler resolution.

The radar comparison included basic Doppler, Multiple Frequency Continuous Wave (MFCW), and Frequency-Modulated Continuous Wave (FMCW) radars. The FMCW radar was eliminated due to its marginal Doppler resolution and higher cost relative to other CW radars. A basic Doppler radar offers both low cost and high Doppler resolution, but the inability to acquire range would most likely affect its classification performance. As a good tradeoff between cost and performance, the Multiple Frequency Continuous Wave (MFCW) radar was chosen. The MFCW radar is the subject of the next section.

#### 4.2 Multiple Frequency Continuous Wave Radar Architecture.

Figure 7 on the next page shows a simplified block diagram of one possible MFCW radar architecture.

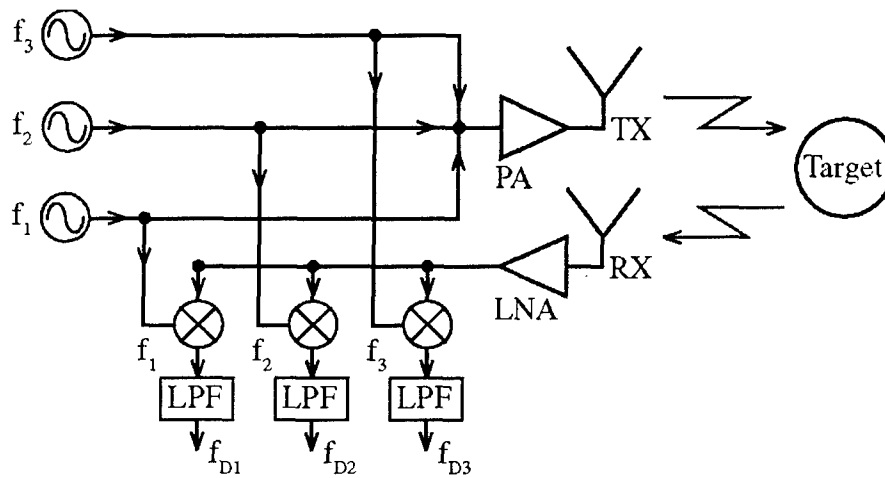


Figure 7. MFCW radar block diagram.

We will refer to the MFCW radar architecture of Figure 7 as a three Frequency Continuous Wave (3 FCW) radar. As the name suggests, the 3FCW radar simultaneously transmits three different frequency tones. Three microwave frequency sources of frequency  $f_1$ ,  $f_2$ , and  $f_3$  provide the required tones. Although not shown in Figure 7, the three frequency sources are all phase-locked to the same crystal reference oscillator. Phase-locked oscillators provide excellent phase noise along with extremely precise frequency spacing between the oscillators. Since all of the oscillators are locked to the same reference source, the oscillators' frequency tends to drift together which maintains the precise frequency separation. The three tones are joined together in a Wilkinson power combiner (shown as a junction in Figure 7) and then passed through a power amplifier before transmission by the antenna. Since the radar is Continuous Wave (CW), one transmit and one receive antenna is used to provide enhanced isolation between the transmitter and receiver.

The 3FCW receiver is a direct-conversion receiver architecture. Thus, the incoming received signal is demodulated directly to baseband without an intermediate frequency. For illustration purposes, let us assume a received signal of the form

$$s_{RX}(t) = \cos(2\pi(f_1 + f_{D1})t) + \cos(2\pi(f_2 + f_{D2})t) + \cos(2\pi(f_3 + f_{D3})t) \quad (13)$$

where  $f_{D1}$ ,  $f_{D2}$ , and  $f_{D3}$  are the Doppler frequencies modulated onto tone one, two, and three respectively. After passing through a low noise amplifier, the received signal power is split equally among the mixers. The signals at the mixers are then demodulated by Local Oscillators (LO) of frequency  $f_1$ ,  $f_2$ , and  $f_3$ . Neglecting the amplitude factors, the output of the mixer that demodulates with LO frequency  $f_1$  is

$$\begin{aligned} \cos(2\pi f_1 t) s_{RX}(t) &= \cos(2\pi f_1 t) \cos(2\pi(f_1 + f_{D1})t) + \cos(2\pi f_1 t) \cos(2\pi(f_2 + f_{D2})t) \\ &\quad + \cos(2\pi f_1 t) \cos(2\pi(f_3 + f_{D3})t) \\ &= \frac{1}{2} \cos(2\pi f_{D1}t) + \frac{1}{2} \cos(2\pi(2f_1 + f_{D1})t) \\ &\quad + \frac{1}{2} \cos(2\pi(f_2 - f_1 + f_{D2})t) + \frac{1}{2} \cos(2\pi(f_2 + f_1 + f_{D2})t) \\ &\quad + \frac{1}{2} \cos(2\pi(f_3 - f_1 + f_{D3})t) + \frac{1}{2} \cos(2\pi(f_3 + f_1 + f_{D3})t) \end{aligned} \quad (14)$$

The mixer outputs six different frequencies along with possibly some other unwanted spurious signals. Low-pass filtering the mixer output isolates the  $\cos(2\pi f_{D1}t)$  term. The maximum expected Doppler frequency controls the choice of filter cutoff frequency. We assume that  $f_{D1}, f_{D2}, f_{D3} \ll (f_2 - f_1), (f_3 - f_1) \ll f_1, f_2, f_3$  so that  $\frac{1}{2}$  so that the sum and difference frequency terms are rejected while the  $\cos(2\pi f_{D1}t)$  term is retained. A similar derivation reveals that the output of the other two mixer/low-pass filter combinations is  $\cos(2\pi f_{D2}t)$  and  $\cos(2\pi f_{D3}t)$ . The receiver outputs three separate Doppler frequency channels.

Although neglected for clarity in Figure 7 and in the previous derivation, the three output channels are actually complex. Each of the three complex output signals contain an inphase (I) and quadrature (Q) component. The resulting complex baseband signal from the first mixer is  $y_{bb1}(t) = I_1 + jQ_1$ . Figure 8 on the next page shows how the I and Q channels are created by what is known as a quadrature demodulator.

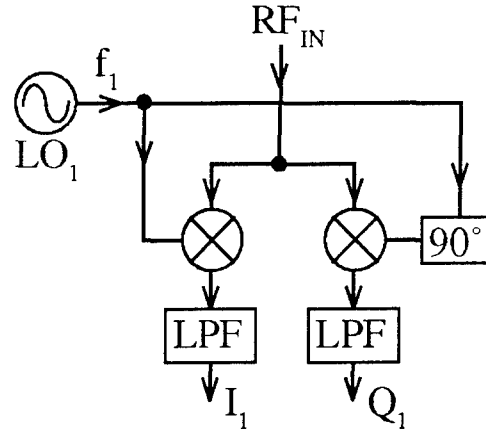


Figure 8. Quadrature demodulator.

Figure 8 reveals that ideally the I and Q channels have the same frequency and amplitude but are  $90^\circ$  out of phase. I/Q error occurs when the I and Q channels are not of equal amplitude or are not exactly  $90^\circ$  out of phase. Correction of I/Q error can be performed either in hardware or software. Software correction will be discussed in a later section of this report. The motivation behind quadrature demodulation is that it preserves the sign of the Doppler frequency. The Doppler frequency shift is positive for targets moving toward the radar and negative for targets moving away from the radar.

#### 4.3 MFCW Radar Target Range Calculation.

As a tradeoff for the best possible Doppler resolution, standard Continuous Wave (CW) radars offer no useful range information. The CW radar's inability to offer useful range information stems from the unambiguous range problem. Let us reconsider Equation (10) which gives the phase of a scattered target pulse at the receiver

$$s_{RX}(t) = \Gamma(t) \exp\left\{j\left[2\pi f_0 t - \frac{4\pi f_0 R(t)}{c} + \psi_0\right]\right\} \quad (15)$$

In principle, the range could be extracted from the return signal by phase comparing the transmit and receive signals [4]. The resulting signal phase is

$$\phi(t) = \frac{4\pi f_0 R(t)}{c} + \psi_0 \quad (16)$$

After removal of the constant phase offset  $\psi_0$  (by calibration), the range becomes

$$R(t) = \frac{c\phi(t)}{4\pi f_0} \quad (17)$$

Since the phase is modulo  $2\pi$ , the range becomes ambiguous when  $\phi(t) = 2\pi m$ , where  $m$  is a positive integer. Thus the range becomes

$$R = \frac{c2\pi m}{4\pi f_0} = \frac{cm}{2f_0} \quad m = 1, 2, 3, \dots \quad (18)$$

The maximum *unambiguous* range,  $R_{unamb}$ , occurs when  $m$  equals 1

$$R_{unamb} = \frac{c}{2f_0} \quad (19)$$

For single-frequency CW radars operating at 10 GHz,  $R_{unamb}$  is 1.5cm. This radar cannot distinguish (for example) whether a target is at 0.5cm, 2cm, 3.5cm, or 150.5cm. For most applications, a maximum unambiguous range of 1.5cm is unacceptable. The Multiple Frequency Continuous Wave (MFCW) radar reduces the unambiguous range problem by simultaneously transmitting multiple tones of slightly different frequencies.

Let us now derive the target range for an MFCW radar. For the MFCW radar where  $M$  is the number of tones, the received signal will be

$$s_{RX}(t) = \sum_{i=1}^M \Gamma_i(t) \exp\{j[2\pi f_i t - \frac{4\pi f_i R(t)}{c} + \psi_i]\} \quad (20)$$

where  $f_i$ ,  $\Gamma_i(t)$ , and  $\psi_i$  are the frequency, amplitude factor, and constant phase offset of the  $i^{\text{th}}$  tone, respectively. After complex demodulation, the phase  $\phi_i(t)$  of the  $i^{\text{th}}$  tone is

$$\phi_i(t) = \frac{4\pi f_i R(t)}{c} - \psi_i \quad (21)$$

The phase difference between tones  $p$  and  $q$  is then

$$\Delta\phi_{p,q}(t) = \frac{4\pi\Delta f_{p,q} R(t)}{c} - \Delta\psi_{p,q} \quad (22)$$

where  $\Delta f_{p,q} = |f_p - f_q|$  is the absolute frequency difference and  $\Delta\phi_{p,q}(t) = \phi_p(t) - \phi_q(t)$  is the phase difference modulo  $2\pi$  between tones  $P$  and  $q$ . The constant phase offset between tones  $p$  and  $q$  is  $\Delta\psi_{p,q} = \psi_p - \psi_q$ . Removal of the phase offset from  $\Delta\phi_{p,q}(t)$  by calibration is necessary to ensure proper range results. One calibrates the radar by comparing the estimated target range with the true range, thus calculating  $\Delta\psi_{p,q}$  in Equation (22). After initial calibration, recalibration is typically not required unless the hardware configuration changes. Following calibration, the range calculated from tones  $P$  and  $q$

$$R_{p,q}(t) = \frac{c\Delta\phi'_{p,q}(t)}{4\pi\Delta f_{p,q}} \quad (23)$$

where  $\Delta\phi'_{p,q}(t)$  is the phase difference after calibration. The range  $R_{p,q}(t)$  becomes ambiguous when  $\Delta\phi'_{p,q}(t) = 2\pi m$  where  $m$  is a positive integer. Hence the maximum unambiguous range due to tones  $P$  and  $q$

$$R_{unamb;p,q} = \frac{c}{2\Delta f_{p,q}} \quad (24)$$

The theoretical root mean square (rms) range error due to tones  $P$  and  $q$  [5]

$$\delta R_{p,q} = \frac{R_{unamb;p,q}}{2\pi(2SNR)^{1/2}} \quad (25)$$

where  $SNR$  is the signal to noise ratio.

Equations (24) and (25) show that both the maximum unambiguous range and range accuracy are inversely proportional to the frequency difference. A tradeoff between maximum unambiguous range and range accuracy occurs if only two transmit frequencies are used. Longer maximum unambiguous range requirements impose coarse range accuracy. This motivates the use of three or more frequencies in MFCW radars. An MFCW radar with more than two tones offers improved unambiguous range and range accuracy. The MFCW radar unambiguous range becomes the maximum of the unambiguous ranges between any two frequency pairs

$$R_{unamb;MFCW} = \max_{p,q} R_{unamb;p,q} \quad (26)$$

After resolving ambiguities [4], the theoretical MFCW rms range error is the minimum error of any two frequency pairs

$$\delta R_{MFCW} = \min_{p,q} \delta R_{p,q} \quad (27)$$

For MFCW radars with three or more tones, the tradeoff for performance enhancement is added system complexity and cost.

For clarification, we will compute the range parameters for the radar design used in this project (three transmit frequencies). Let tone one with frequency  $f_1$  and tone two with frequency  $f_2$  be two tones closely spaced in frequency. Tone three with frequency  $f_3$  is spaced farther apart from tone one than tone two as illustrated in Figure 9 below.

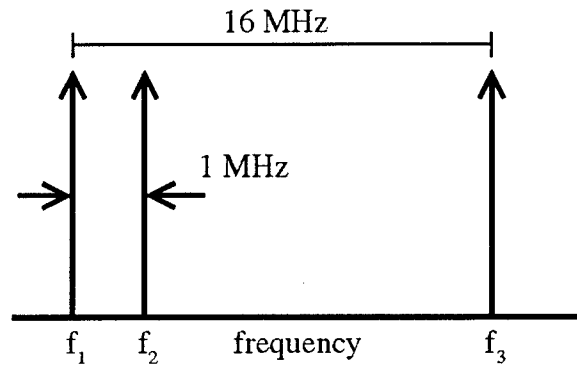


Figure 9. Three tone frequency separation.

Tones one and two provide a long unambiguous range while tones one and three offer an accurate but ambiguous range. Table 2 on the next page lists the parameters for this example.

Table 2. Ranging parameters.

Parameter	Value	Parameter	Value
$\Delta f_{1,2}$	1 MHz	$R_{unamb;1,2}$	150 m (492 ft)
$\Delta f_{1,3}$	16 MHz	$R_{unamb;1,3}$	9.375 m (30.76 ft)
$f_1$	10 GHz	$\delta R_{1,2}$	3.568 m (11.71 ft)
SNR	13.5 dB	$\delta R_{1,3}$	0.223 m (0.732 ft)

The tones separated by 1MHz give an unambiguous range of 150m while the 16MHz separated tones provide 0.223m range accuracy. The range accuracy calculations used 13.5dB as the SNR.

## Section 5

### Target Detection and Ranging

#### 5.1 Radar Range Equation.

The calculation of fundamental radar design parameters from system requirements typically starts with the use of the radar range equation. One of many forms of the radar range equation is

$$R_{\max} = \left[ \frac{G_t G_r P_t \lambda^2 \sigma}{(4\pi)^3 k T_0 B F SNR_{\min} L} \right]^{1/4} \quad (28)$$

where  $G_t$  = transmitting antenna gain  $G_r$  = receiving antenna gain  
 $P_t$  = transmit power  $\lambda$  = wavelength of transmit signal  
 $\sigma$  = target radar cross section = Boltzmann's constant ( $1.38 \times 10^{-23}$  J/K)  
 $T_0$  = room temperature (290K) = receiver bandwidth  $B$   
 $F$  = receiver noise figure = system loss factor  $L$   
 $SNR_{\min}$  = minimum signal to noise ratio required for detection

Equation (28) calculates the maximum detectable range to a target of Radar Cross Section (RCS). The radar range equation is an over-simplification of a complex problem, but it gives the system designer a good starting point. One notable simplification is that the RCS value is a constant. A target's RCS varies with aspect angle, frequency, and polarization. This form of the radar range equation also neglects received signal fluctuation due to dynamic propagation effects such as multipath.

Equation (28) in its current form gives no direct information as to the reliability of detection. The parameters that describe detection reliability (probability of detection and false alarm) are contained in the  $SNR_{\min}$  term. In the next section, we will review the important concepts of classical detection theory to explicitly express  $SNR_{\min}$  in terms of probability of detection and false alarm.

## 5.2 Classical Detection Theory.

Signal detection is a classical problem of binary statistical hypothesis testing. Under the null hypothesis, the complex baseband received signal is composed of noise alone.  $H_0 y(t)$

$$H_0: y(t) = n(t) \quad \text{where} \quad n(t) = n_I(t) + jn_Q(t) \quad (29)$$

We assume the predominant noise source is thermal, so both the inphase and quadrature noise components are Gaussian. Under hypothesis, the received signal is the sum of the transmitted signal and noise.  $H_1 y(t) s(t)$

$$H_1: y(t) = s(t) + n(t) \quad \text{where} \quad s(t) = s_I(t) + js_Q(t) \quad (30)$$

Let  $I$  and  $Q$  be the inphase and quadrature components of, respectively. For this development, we assume the received signal is processed by a linear detector  $y(t)$ :

$$V = \sqrt{I^2 + Q^2} \quad (31)$$

where is the complex envelope of the baseband signal.  $I$  and  $Q$  are independent Gaussian random variables under hypothesis, so we arrive at the well-known result that the envelope  $V$  is Rayleigh distributed  $H_0$

$$p_{V|H_0}(v|H_0) = \frac{v}{\sigma^2} \exp\left[-\frac{v^2}{2\sigma^2}\right] \quad (32)$$

where  $\sigma^2$  is the conditional variance and  $p_{V|H_0}(v|H_0)$  is the conditional probability density function of  $V$  given that the received signal is only noise (). Equation  $H_0$  (32) depends on the single parameter  $\sigma^2$ . Estimation of  $\sigma^2$  is facilitated by the following relation

$$\sigma = \sqrt{\frac{2}{\pi}} E[V|H_0] \quad (33)$$

where  $E[V|H_0]$  is the conditional expected (mean) value of  $V$  given  $H_0$

S.O. Rice showed that under hypothesis, the envelope  $V$  takes on the Ricean distribution [6]  $H_1$

$$p_{V|H_1}(v|H_1) = \frac{v}{\sigma_{V|H_1}^2} \exp\left[-\frac{(v^2 + A^2)}{2\sigma_{V|H_1}^2}\right] I_0\left(\frac{vA}{\sigma_{V|H_1}^2}\right) \quad (34)$$

where  $I_0(\cdot)$  is the modified Bessel function of zero order. Here  $\sigma_{V|H_1}^2$  is the conditional variance and  $p_{V|H_1}(v|H_1)$  is the conditional probability density function of  $V$  given that the received signal is a sinusoidal signal of amplitude  $A$  plus noise. Figure 10 below shows the probability density functions under  $H_0$  and  $H_1$ .

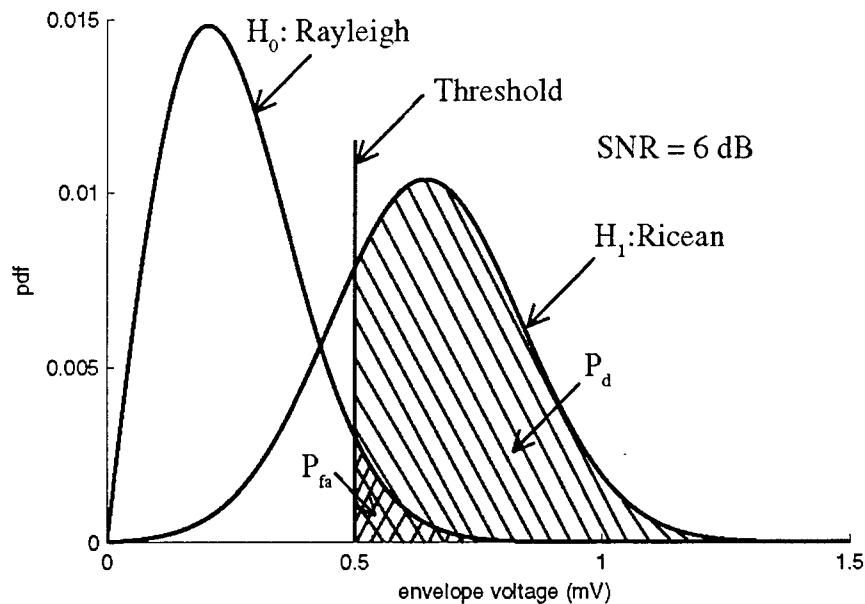


Figure 10. Probability density functions of noise and signal plus noise.

Two types of errors can occur in the detection problem. A type 1 error, commonly known as a false alarm, happens when no signal is present but the noise level exceeds the detection threshold. A type 2 error, known as a missed detection, occurs when a signal is present but the signal level is not high enough to cross the detection threshold. Intuition would tell us that we want to simultaneously minimize both types of errors. The total error is minimized in the ideal observer detection criterion [5]. This detection methodology often works well in communications systems where the cost of making either type of error is typically equal. However, in radar systems the ideal observer criterion results in high false alarm rates. The Neyman-Pearson detection criterion provides a method of detection that is well suited to the radar problem.

In the Neyman-Pearson detector, the probability of false alarm  $P_{fa}$  is fixed, while the probability of missed detection is minimized. Equivalently, the probability of detection is maximized since  $P_m P_c P_d = 1 - F$ . The probability of false alarm is typically fixed by system requirements on the minimum tolerable time between false alarms. For continuous-time detection, it can be shown [5] that the probability of false alarm is related to the average time between false alarms by

$$P_{fa} = \frac{1}{T_{fa} B} \quad (35)$$

where  $T_{fa}$  is the average time between false alarms and  $B$  is the receiver noise bandwidth (roughly approximated by the 3dB bandwidth of the pre-detection filters). Once the system designer determines the noise bandwidth, the probability of false alarm is fixed by the required average time between false alarms.  $B$

The detection threshold is easily obtained once the probability of false alarm is set. As seen in Figure 10, the probability of false alarm is the area under the noise-only curve above the threshold level  $\gamma$ .

$$P_{fa} = \int_{\gamma}^{\infty} p_{v|H_0}(v|H_0)dv = \int_{\gamma}^{\infty} \frac{v}{\sigma^2} \exp\left[-\frac{v^2}{2\sigma^2}\right] dv = \exp\left[-\frac{\gamma^2}{2\sigma^2}\right] \quad (36)$$

Solving for  $\gamma$  yields

$$\gamma = \sigma \sqrt{2 \ln\left(\frac{1}{P_{fa}}\right)} \quad (37)$$

If the noise statistics are not time-varying, the threshold  $\gamma$  maintains the specified probability of false alarm while maximizing the probability of detection. In order to maintain a constant probability of false alarm in the presence of non-stationary noise, an adaptive threshold method such as the Constant False Alarm Rate (CFAR) detector is required.

As shown in Figure 10, the probability of detection is the area under the signal-plus-noise curve above the detection threshold

$$P_d = \int_{\gamma}^{\infty} p_{v|H_1}(v|H_1)dv = \int_{\gamma}^{\infty} \frac{v}{\sigma^2} \exp\left[-\frac{(v^2 + A^2)}{2\sigma^2}\right] I_0\left(\frac{vA}{\sigma^2}\right) dv \quad (38)$$

The integral of Equation (38) cannot be solved by traditional analytical techniques. The numerical solution of Equation (38) is [7]

$$P_d = \frac{1}{2} \operatorname{erfc} \left( \sqrt{-\ln(P_{fa})} - \sqrt{\operatorname{SNR} + \frac{1}{2}} \right) \quad (39)$$

where  $\operatorname{erfc}(\bullet)$  is the complimentary error function. Solving for SNR gives

$$\operatorname{SNR} = \left( \sqrt{\ln \left( \frac{1}{P_{fa}} \right)} - \operatorname{erfc}^{-1}(2P_d) \right)^2 - \frac{1}{2} \quad (40)$$

where  $\operatorname{erfc}^{-1}(\bullet)$  is the inverse complimentary error function. Figure 11 on the next page plots the Receiver Operating Curve (ROC), a family of solutions to Equation (39).

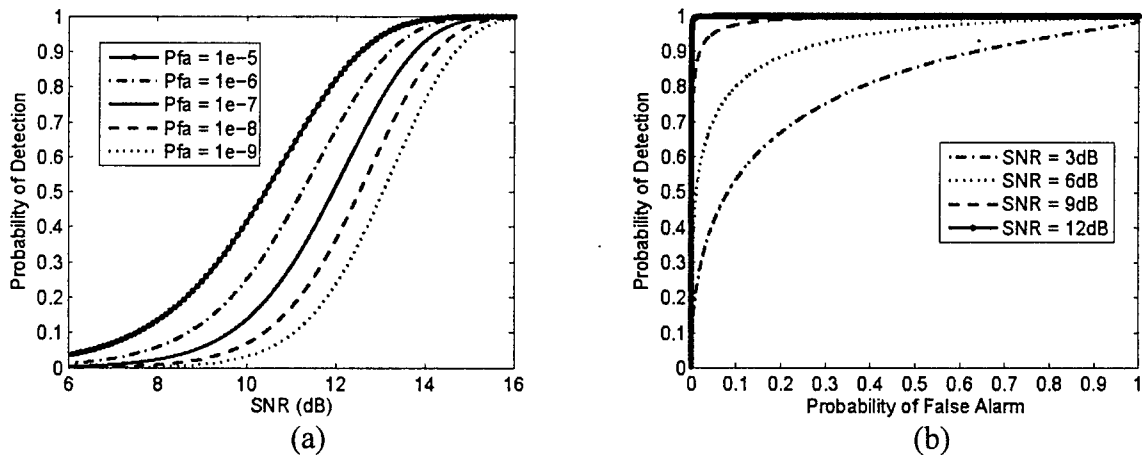


Figure 11. Probability of detection versus SNR (a) and receiver operating curve (b).

Figure 11(a) provides a quick view of the impact of varying system requirements on the required SNR. Lowering the false alarm rate (increasing the average time between false alarms) results in higher required SNRs for the same probability of detection. Also, if the required probability of detection is reduced while maintaining the same false alarm rate, lower SNRs are required.

Equation (40) can now be substituted into Equation (28) to get a radar range equation which explicitly includes detection reliability terms

where  $R_{\max; P_d, P_b, \sigma}$  is the maximum range to a target of radar cross section  $\sigma$ ,

(41)

given that the required probability of detection is  $P_d$  and the required probability of false alarm is  $P_b$ . It is important to remember that Equation (41) is still an approximation to the maximum range because of received signal and noise statistical fluctuations. The effects of fluctuations can be reduced by averaging (integrating) the received signal over a short time window.

### 5.3 Detection in the Joint Time-Frequency Domain.

The detection method described in the previous section historically has been performed in either the time or frequency domains. Recently, joint time-frequency domain detection has received increasing attention [2], [8], [9]. The reason for the peak in interest is attributed to the fact that uncorrelated noise spreads out over the time-frequency domain, while frequency-modulated signals tend to localize. With a suitably defined SNR [2], the joint time-frequency domain SNR will be greater than (or equal to in certain cases [9]) the SNR in either the time or frequency domains. Since Doppler radar signatures primarily consist of frequency-modulated components, performance is likely to improve by detecting in the joint time-frequency domain.

The detection theory developed in Section 5.2 is still valid in the time-frequency domain if we make some adjustments. Equation (31) for the received signal envelope should be changed to

$$V_{k,n} = \sqrt{(\text{Re}[C_{k,n}])^2 + (\text{Im}[C_{k,n}])^2} \quad (42)$$

where  $\text{Re}[C_{k,n}]$  and  $\text{Im}[C_{k,n}]$  are the real and imaginary parts of time-frequency coefficient  $C_{k,n}$ . In the time-frequency domain, the probability of false alarm  $P_{fa}$  and the probability of detection  $P_d$  are now specified per spectrogram "pixel." In other words,  $P_{fa}$  should be interpreted as the probability that a single time-frequency bin false alarms. To reduce the overall system false alarm probability  $P_{fa,sys}$ , a radar system would likely not report an alarm unless more than a single time-frequency bin was detected. We will refer to  $P_{fa}$  as the probability of *pixel* false alarm and  $P_{fa,sys}$  as the probability of *system* false alarm. Let us now derive the probability of system false alarm.

Each column of a spectrogram corresponds to an  $N$ -point Fast Fourier Transform (FFT) of a windowed segment of data. One method of reducing the overall system false alarm rate is to require a minimum number of detected pixels within a given FFT before signaling a system alarm. If we require at least  $N_z$  pixels to set a system alarm, the probability of system false alarm is the probability that  $N_z$  or more pixels cross the detection threshold when no target is present.

Let  $M$  be one of  $N$  FFT points following *pixel-level* detection. If no target is present,  $M$  takes on a Bernoulli distribution of parameter  $P_{fa}$

$$f_M(m) = P_{fa}^m (1 - P_{fa})^{N-m} \quad \text{where } m \in \{0, 1, \dots, N\} \text{ and } P_{fa} \in [0, 1] \quad (43)$$

where  $f_M(m)$  is the Bernoulli probability mass function of  $M$ . Hence, with probability  $P_{fa}$ ,  $M$  is a false alarm, and with probability  $(1 - P_{fa})$ ,  $M$  is not a false alarm. Suppose we want to find the probability that exactly  $r$  (independent) pixels false alarm in  $N$  trials. The binomial distribution gives this probability for fixed  $r, N$

$$P(R=r) = f_{RN}(r|N) = \binom{N}{r} P_{fa}^r (1 - P_{fa})^{N-r} \quad (44)$$

where  $P(\cdot)$  is a suitable probability measure and  $\binom{N}{r}$  is a binomial coefficient. To determine the probability of system false alarm  $P_{fa,sys}$ , we need to know the probability that  $N_z$  or more pixels false alarm.

We then have

$$P_{fa,sys} = P(R \geq z | N) = \sum_{j=z}^N \binom{N}{j} P_{fa}^j (1 - P_{fa})^{N-j} = I_{P_{fa}}(z, N - z - 1) \quad (45)$$

where  $I_x(a, b)$  is the regularized incomplete beta function [10].

In a system design, the designer calculates the probability of system false alarm from the specified minimum average time between false alarms. If  $T_{FFT}$  is the time in seconds between

consecutive FFTs, the number of *system-level* detection decisions per second is  $\frac{1}{T_{FFT}}$ . The minimum average time between false alarms,  $T_{fa,sys}$ , is then

$$T_{fa,sys} = \frac{T_{FFT}}{P_{fa,sys}} \quad (46)$$

After calculating  $P_{fa,sys}$  from  $T_{fa,sys}$ , the designer obtains  $P_{fa}$  from

$$P_{fa} = I_{P_{fa,sys}}^{-1}(z, N - z + 1) = I_{\frac{T_{FFT}}{T_{fa,sys}}}^{-1}(z, N - z + 1) \quad (47)$$

where  $I_x^{-1}$  is the inverse regularized incomplete beta function [11]. The probability of pixel false alarm is then used to find the minimum required signal to noise ratio. Table 3 on the next page lists the parameters for the radar system used in this project.  $I_{P_{fa,sys}}^{-1}(z, N - z + 1)$

Table 3. Detection parameters.

Name	Symbol	Value
mean time between false alarms	$T_{fa,sys}$	<u>7 days</u>
time between each FFT	$T_{FFT}$	<u>38.5ms</u>
required number of pixels for alarm		
probability of system false alarm	$P_{fa,sys}$	<u><math>6.37 \times 10^{-8}</math></u>
probability of pixel false alarm	$P_{fa}$	<u><math>3.49 \times 10^{-7}</math></u>
probability of detection	$P_a$	<u>0.9</u>
minimum SNR required for detection	$SNR_{min,P_d,P_{fa}}$	<u>13.5dB</u>

Starting with a specification of 7 days between system false alarms, we calculate that . For a requirement of 0.9 probability of detection, the minimum SNR for detection is 13.5dB (see Section 5.2).  $P_{fa} = 3.49 \times 10^{-7}$ .

Requiring  $z$  or more pixels for detection to reduce the false alarm rate does not go without penalty. Suppose that  $z$  equals 2 and  $P_a$  equals 0.9. If target signal energy appears in only one frequency bin, the radar has no chance of detecting the target. If at  $P_a$  least two frequency bins contain target energy (at the minimum SNR), the probability of system-level detection increases to approximately 0.81 (assuming independent samples). When there are at least three frequency bins, the system-level detection probability increases to approximately 0.97. In general, if  $Q$  independent frequency bins contain target energy at the minimum required SNR, the system-level probability of detection is  $P_d^{(z)} = I_{P_a}(z, Q - z - 1)$

$$P_{d,sys} = \sum_{j=z}^Q \binom{Q}{j} P_d^j (1 - P_d)^{Q-j} = I_{P_a}(z, Q - z - 1) \quad (48)$$

Although probability of detection loss occurs for narrowband targets (targets whose frequency spread is on the order of the frequency resolution), the benefits of reduced probability of system false alarm far outweigh this loss (primarily since the targets of interest to this project are moderately wideband due to micro-Doppler).

#### 5.4 Procedure for Joint Time-Frequency Domain Detection.

Figure 12(a) on the next page shows the spectrogram of a human target. The target jogs toward the radar going from a range of 100ft to 50ft and then turns around and jogs back to 100ft.

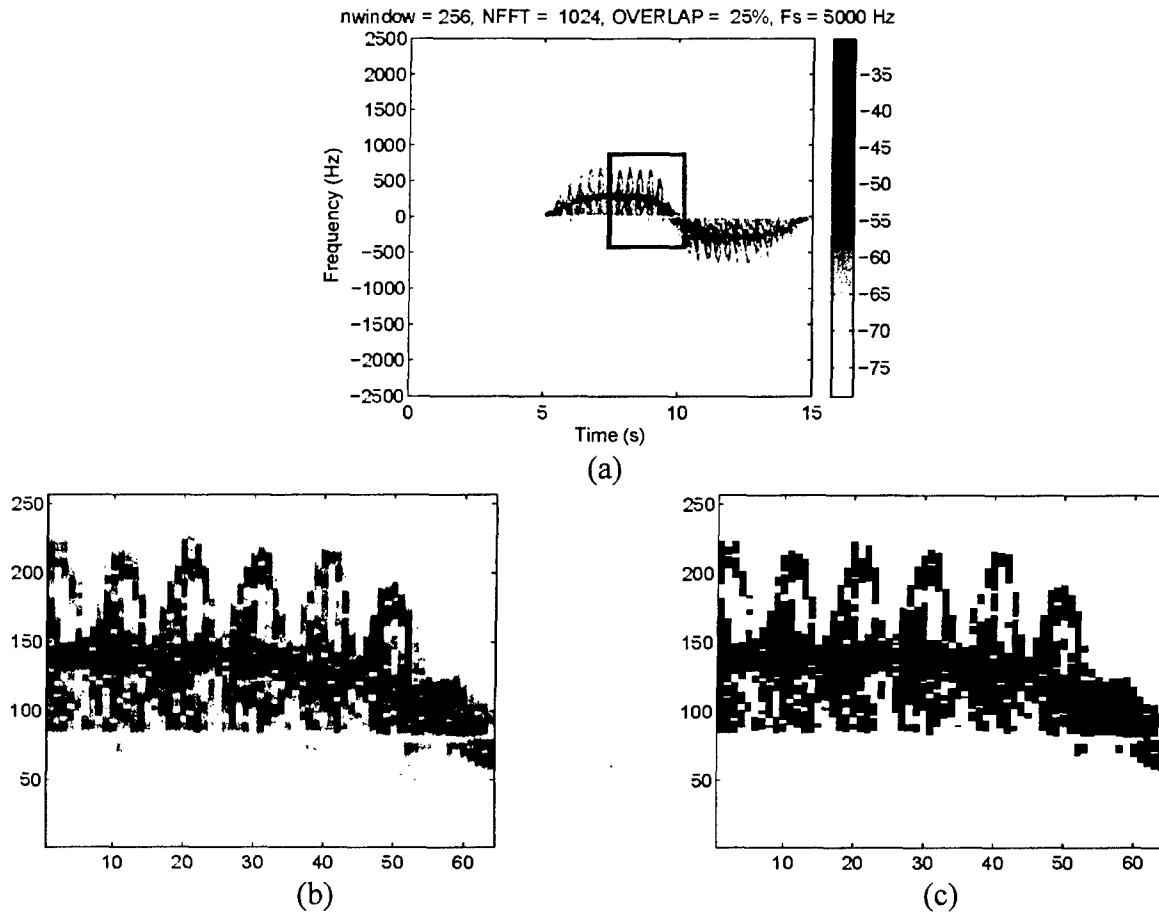


Figure 12. Complete spectrogram (a), extracted frame (b), and detected frame (c).

The detection procedure starts by extracting a frame (typically 1,250Hz by 2.46s) centered on the largest spectrogram return within a given time frame (see Section 5.5 for target tracking). An extracted frame is shown in Figure 12(b). Each pixel within the frame is compared with a threshold to determine if noise or target energy is present within that pixel. Figure 12(c) displays the detected frame for a threshold of -61dBm. The detected frame shows good detection of the target torso along with the micro-Doppler produced by the legs and arms.

Figure 13 on the next page illustrates the effect of varying the detection threshold on pixel false alarms and missed detections.

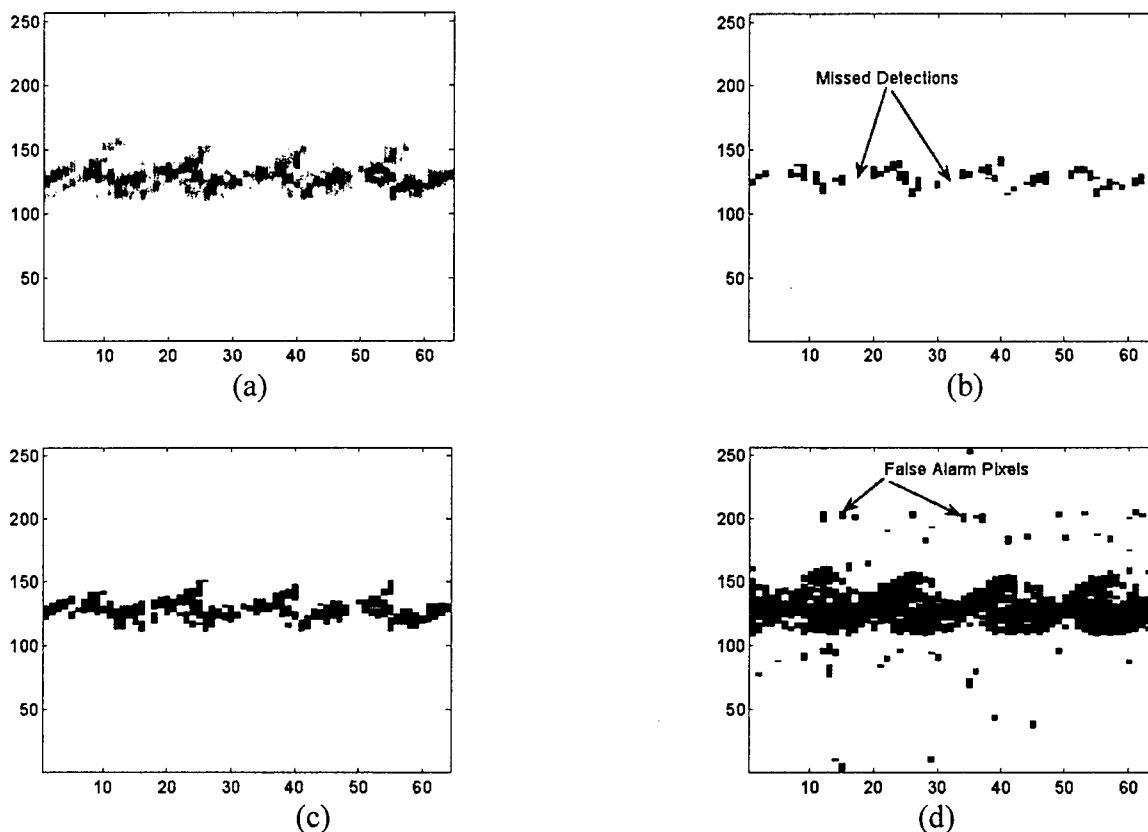


Figure 13. Spectrogram frame for human target (a), detection results for threshold level: -55dBm (b), -61dBm (c), and -76dBm (d).

Figure 13(a) is a spectrogram frame of a human target walking toward the radar at a range of approximately 225ft. In Figure 13(b) the detection threshold is set to -55dBm. No pixels false alarm within this detection frame, but numerous missed detections occur. In Figure 13(d), a much higher threshold of -76dBm is used. This threshold dramatically increases the number of false alarm pixels but considerably decreases the number of missed detections. The threshold of -61dBm used in Figure 13(c) makes a good compromise between false alarm and missed detection pixels.

## 5.5 Ranging in the Joint Time-Frequency Domain.

In Section 4.3, we calculated the MFCW radar target range from the phase difference between any pair of tones. An analog phase comparator could be used to extract the phase difference between two Doppler channels. However, if we wanted to resolve multiple targets by their Doppler frequencies, a phase comparator would need to be placed on each output of a Doppler filter bank (unless one time-shared filter is to be used). The expense and complexity of such a system grows rapidly as the requirement for finer Doppler resolution tightens. Another option is to calculate the phase difference digitally in software. One could perform a phase estimate in the time domain, but the ability to resolve multiple targets by Doppler would be lost. In this project, the phase difference estimate is performed in the joint time-frequency domain.

Since we are already using the STFT magnitude (spectrogram) to perform detection and signature extraction, the STFT phase provides the phase difference estimate with little extra computation. The STFT can be split up into magnitude and phase components

$$STFT_x[k, n] = |STFT_x[k, n]| \angle STFT_x[k, n] \quad (49)$$

If we let  $\text{Re}[C_{k,n}]$  and  $\text{Im}[C_{k,n}]$  be the real and imaginary parts of time-frequency coefficient  $C_{k,n}$ , we get

$$\begin{aligned} |STFT_x[k, n]| &= \sqrt{(\text{Re}[C_{k,n}])^2 + (\text{Im}[C_{k,n}])^2} \\ \angle STFT_x[k, n] &= \tan^{-1} \left[ \frac{\text{Im}[C_{k,n}]}{\text{Re}[C_{k,n}]} \right] \end{aligned} \quad (50)$$

where the inverse tangent must be a four quadrant operation for proper results. The phase difference between tones  $p$  and  $q$  at frequency index  $k$  and time index  $n$  is

$$\Delta\phi_{p,q}[k, n] = \angle STFT_p[k, n] - \angle STFT_q[k, n] \quad \text{where } \Delta\phi_{p,q}[k, n] \in [0, 2\pi] \quad (51)$$

In order to ensure that  $\Delta\phi_{p,q}[k, n] \in [0, 2\pi]$ , the arithmetic for the phase calculation must be modulo  $2\pi$ .

The phase difference between tones  $P$  and  $Q$  gives

$$R_{p,q}[k,n] = \frac{c\Delta\phi_{p,q}[k,n]}{4\pi\Delta f_{p,q}} \quad (52)$$

where  $R_{p,q}[k,n]$  is the range estimate at frequency index  $k$  and time index  $n$ . To prevent adding bias to  $knR_{p,q}[k,n]$ , it is important to remove any constant phase offset from  $\Delta\phi_{p,q}[k,n]$  (by range calibration) prior to calculating  $R_{p,q}[k,n]$ .

We introduce the Time-Frequency-Range Diagram (TFRgram) as the time-frequency-range image of  $R_{p,q}[k,n]$ . Figure 14 below plots the TFRgram and spectrogram of a human target jogging from 292 feet to 15 feet.

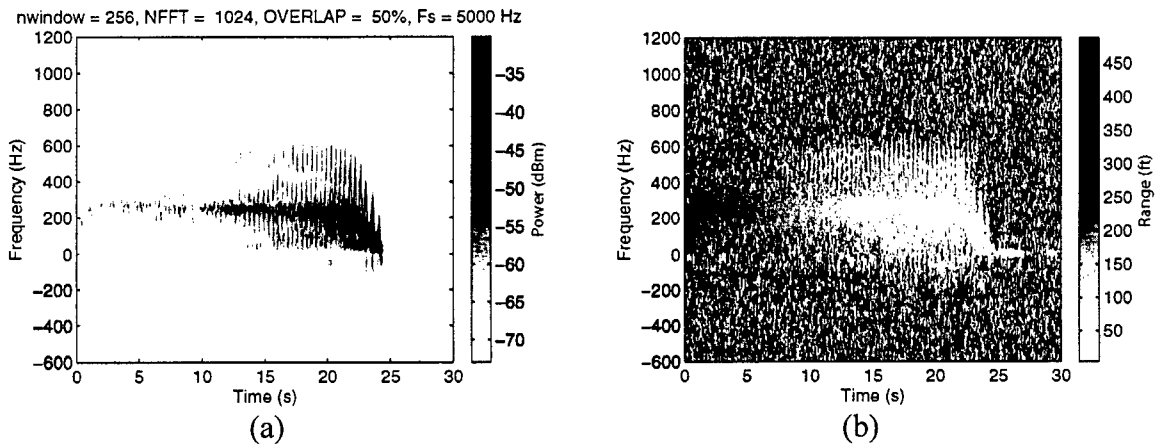


Figure 14. Spectrogram (a) and TFRgram (b) of human jogging from 292ft to 15ft .

The TFRgram is similar to a spectrogram in that the target is located in the same time-frequency bins, however the color axis plots range instead of power. As expected, the range appears random in regions of the time-frequency plane where no target is present. Valid estimates of target range only come from regions of  $R_{p,q}[k,n]$  with target signal energy. Further processing is required to extract the target range from the TFRgram.

In order to acquire useful range estimates from the TFRgram, the frequency coordinates of the target must be found. The frequency coordinates select the proper region of the TFRgram to extract range information. Note that due to the Doppler effect, the frequency coordinates are proportional to the target velocity relative to the radar.

One possible extraction method calculates the frequency location of the maximum value of the spectrogram at each time instant

$$k_{\text{target}}[n] \Big|_{n=n_0} = \underset{k}{\operatorname{argmax}} \left[ |STFT_x[k, n]|^2 \Big|_{n=n_0} \right] \quad (53)$$

where  $k$  is the frequency coordinate of the target at time  $n$ . A scaled version of  $k_{\text{target}}[n]$  is plotted below in Figure 15(a) for the human target of Figure 14.  $k_{\text{target}}[n]$  is  $n k_{\text{target}}[n]$  is

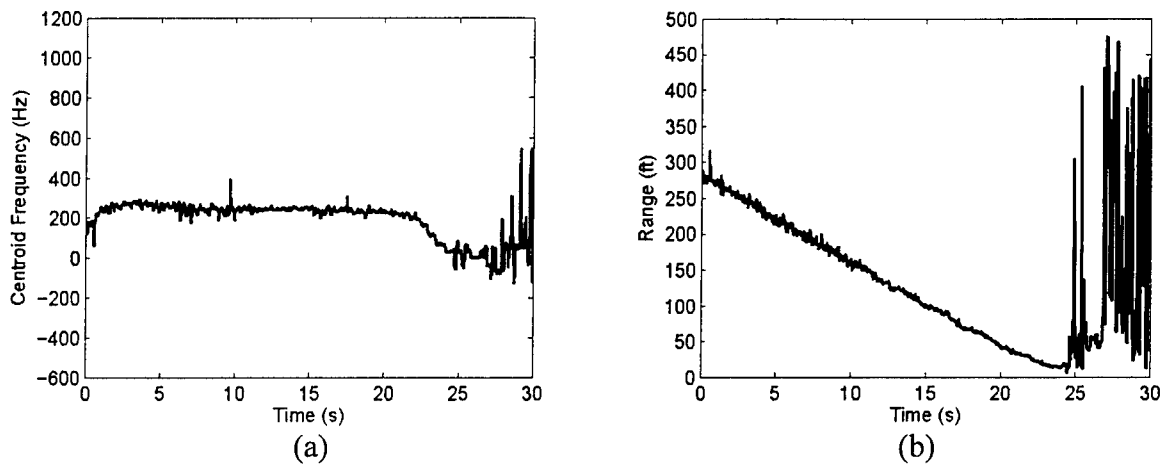


Figure 15. Centroid frequency (a) and target range (b).

The target frequency coordinate is tracked reasonably well until the target stops moving at about the 25 second mark. The frequency coordinate should be zero here, but instead the value fluctuates rapidly due to signal loss. This discrepancy can be corrected by zeroing the frequency coordinate at any time instant that no signal is detected.

Figure 15(b) shows the target range extracted from the TFRgram using the frequency coordinates of Figure 15(a). Two tones separated in frequency by 1MHz were used for this calculation. Since rms range accuracy improves with increasing SNR, the range estimate fluctuates less as the target approaches the radar. In Figure 15(b), the range estimate varies wildly after the target stops moving. This problem can be alleviated by keeping the range estimate constant over time intervals with no signal detections.

## Section 6 Radar Hardware Design

### 6.1 Radar System Design.

Most radar system designs begin with a list of specifications such as those of Table 1. A radar designer then typically consults an appropriate range equation to determine which parameters are fixed by specifications and which parameters the designer can manipulate. The range equation we will use for our analysis will be Equation (41) of Section 5.2 repeated below.

$$R_{\max, P_d, P_{fa}, \sigma} = \left[ \frac{G_t G_r P_t \lambda^2 \sigma}{(4\pi)^3 k T_0 B F \left\{ \left( \sqrt{\ln \left( \frac{1}{P_{fa}} \right)} - \operatorname{erfc}^{-1} (2P_d) \right)^2 - \frac{1}{2} \right\} L} \right]^{1/4} \quad (54)$$

The radar range equation in this form contains 11 variables. Two of the 11 variables are strictly fixed by system specifications: the probability of detection and the maximum range to a target of RCS  $P_a \sigma$  (given  $P_{fa}$  and  $P_d R_{\max, P_d, P_{fa}, \sigma}$ ). As discussed in Section 5.3, the probability of pixel false alarm  $P_{fa}$  is determined by the specification of minimum average time between system false alarms. The average RCS  $\sigma$  is typically set by the choice of transmit frequency and the radar targets of interest. Among the remaining variable parameters are the antenna gains, the transmit power, the transmit wavelength  $G_t$  and  $G_r P_t \lambda$ , the receiver bandwidth, the receiver noise figure, and the aggregate system losses.  $BFL$

An important stage of the radar design cycle is to enumerate the primary factors that influence parameter selection. Table 4 below lists the main inter-dependencies among the parameters.

Table 4. Factors influencing design parameter selection.

Design Parameter	Symbol	Primary Influential Factors
transmit wavelength	$\lambda$	cost, Doppler resolution, FCC, size
baseband bandwidth		transmit wavelength, max target speed
transmit power	$P_t$	cost, power consumption, FCC, size
antenna gain	$G_t, G_r$	cost, angular coverage, size
receiver noise figure		cost, power consumption, size
system losses		cost, power consumption, size

For a specific design, several of the influencing factors of Table 4 may not be of high importance. Size and power consumption constraints were of minor concern to the radar design in this project, while Doppler resolution and cost heavily influenced the design. In the next section, we further discuss Table 4 and MFCW radar system design.

## 6.2 MFCW Radar Design.

In this section, we narrow the design focus to an MFCW radar used for collection of high Doppler resolution target signatures. Since Doppler resolution improves with increasing frequency, shorter transmit wavelengths are favored. However, obtaining inexpensive radar components past X-band (8-12GHz) is difficult. Since cost is a significant factor to this project, a 3cm operating wavelength (10GHz frequency) was chosen as a tradeoff of cost and Doppler resolution. After selecting a transmit frequency, the receiver bandwidth is determined by the maximum expected target speed. If the maximum expected target speed is 35 meters per second (78 mph), the maximum Doppler frequency received (for a 10GHz transmit frequency) is approximately 2.35kHz. The chosen sampling rate is 5kHz, which is slightly higher than the Nyquist rate. The sampling rate then sets the baseband bandwidth to be roughly equal to twice the 3dB bandwidth of the anti-aliasing filters. For this project, the complex baseband bandwidth is approximately 5kHz.

Cost, power, and size constraints typically dictate the selection of transmit power. In addition, the Federal Communications Commission (FCC) sets limits on the maximum radiated power density which factors into some high power budget designs. Cost is the main limitation on transmit power for this project. Low cost power amplifiers from Hittite Microwave Corporation (HMC) offer moderate output power from a small, low power package. The power amps from HMC achieved excellent linearity at 16dBm (40mW) transmit power.

For aperture-type antennas, the antenna size and gain are inversely proportional to the beamwidth. Thus, antenna selection is often dominated by angular coverage requirements and size (and/or weight) limits. Inexpensive, compact 17dB gain horn antennas were selected for this design. The antenna beamwidth is 25° in both the azimuth and elevation planes. Optimization of system noise figure and overall system losses within system requirements is a significant design challenge. In the next section, we discuss system design for reduced noise figure.

### 6.3 System Design For Reduced Noise Figure.

Noise figure refers to the reduction of signal to noise ratio from the input to the output of a device. One then defines the noise figure as

$$F = \frac{SNR_{in}}{SNR_{out}} \quad (55)$$

where and are the input and output signal to noise ratios, respectively. Implicit in the definition of noise figure is that the input noise to the device results from a matched (to the system characteristic impedance) resistor at a temperature of 290K. Receiver design relies heavily on noise figure optimization. To use noise figure in receiver design, one must determine the overall noise figure of the cascaded devices within the receiver. Cascading N devices results in an overall noise figure of  $SNR_{in} SNR_{out}$

$$F = F_1 + \frac{F_2 - 1}{G_1} + \frac{F_3 - 1}{G_1 G_2} + \dots + \frac{F_N - 1}{G_1 G_2 \dots G_N} = F_1 + \sum_{i=2}^N \frac{F_i - 1}{\prod_{j=1}^{i-1} G_j} \quad (56)$$

where is the noise figure and is the gain of the  $i^{th}$   $F_i G_i$  device. Since the gain of previous stages reduces the effective noise figure of a device, the first few components of a receiver chain typically contribute the most to the overall system noise figure. Therefore, judicious placement of receiver front-end components can dramatically affect system noise levels.

The noise figures and gains of the front-end components used in this project' design are listed in Table 5 on the next page.

Table 5. Front-end component noise figures and gains.

	Low Noise Amp	Power Divider	Balanced Mixer
Noise Figure	2.5 dB	3.7dB	8.5dB
Gain	15dB	-3.7dB	-8.5dB

In addition to the components of Table 5, we assume a coaxial cable and connector loss at the input to the receiver of 0.5dB. This input loss constrains the first stage noise figure to be 0.5dB. For a 3FCW radar using quadrature demodulation, the received signal must be power-divided three times before reaching the mixers. The three power splits combine to give a rather large 11dB power splitter loss. In practice, power splitter loss limits the number of tones used in an MFCW radar. Figure 16 below shows one possible receiver front end configuration.  $F_1$

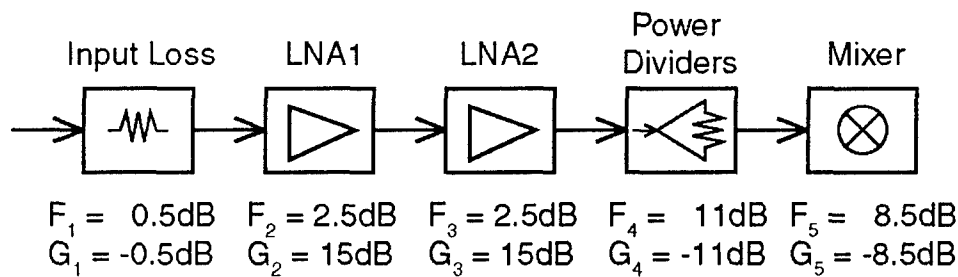


Figure 16. Receiver front end with two LNAs before the power dividers.

The receiver front end of Figure 16 provides 10dB overall gain and 3.3dB noise figure. Other noise figures can be achieved by varying the position and number of Low Noise Amplifiers (LNAs) as seen in Table 6 on the next page.

Table 6. Varying receiver specifications by changing number and position of LNAs.

# of LNAs	LNA Position	Noise Figure	Gain
0	n/a	20 dB	-20 dB
1	after dividers	14.4 dB	-5 dB
1	before dividers	7.1 dB	-5 dB
2	after dividers	14.1 dB	10 dB
2	before dividers	3.3 dB	10 dB

Table 6 clearly shows the benefit of positioning the LNAs before the power dividers. Adding more LNAs improves the noise figure, but too many LNAs will deteriorate the receiver dynamic range along with cost and power budgets.

### 6.3 Analog to Digital Converter Limitations On Noise Floor.

The receiver noise floor referenced to the receiver input is defined as

$$P_N \triangleq kT_0BF \quad (57)$$

where  $k$  is Boltzmann's constant,  $T_0$  is 290K,  $B$  is the detection bandwidth, and  $F$  is the receiver noise figure. An  $n$ -bit Analog to Digital Converter (ADC) with a full-scale voltage range of  $kT_0BFV_{fs}$  will have a resolution of

$$\Delta V = \frac{V_{fs}}{2^n} \quad (58)$$

Quantization noise takes on a uniform probability density between  $-\frac{\Delta V}{2}$  and  $\frac{\Delta V}{2}$ , so the noise variance becomes [12]

$$\sigma_N^2 = \frac{\Delta V^2}{12} \quad (59)$$

For a system with characteristic impedance  $Z_0$ , the ADC noise power is

$$P_N = \frac{\sigma_N^2}{Z_0} \quad (60)$$

The ADC noise power referenced to the input of a receiver of gain  $G$  becomes

$$P_{N,ADC} = \frac{P_N}{G} = \frac{1}{G} \cdot \frac{\Delta V^2}{12Z_0} \quad (61)$$

For a receiver with  $F = 3.3\text{dB}$ ,  $B = 5\text{kHz}$ , and  $G = 36\text{dB}$  (gain including baseband amplification) the noise floor is  $(-134\text{dBm})$ . However, the noise power of a  $\pm 1\text{V}$  range 16-bit ADC referred to this receiver's input is much higher at  $(-110\text{dBm})$ . Therefore, the 16-bit ADC sets the noise-floor in this project's design. A 16-bit ADCs was chosen because they are inexpensive and are common on DSPs and microcontrollers.

$$F B 4.28 \times 10^{-17} W \pm 59.75 \times 10^{-15} W$$

## Section 7 Database Collection and Processing

### 7.1 Experimental Setup.

Following the completion of the last radar hardware revision, an extensive database of radar signatures was collected over an eight month period in 2004. Most of the radar tests were performed in an urban environment as seen in Figure 17 below.



Figure 17. Urban testing environment.

Several buildings, a concrete driveway, and parked vehicles all contributed to the complex multipath propagation environment. Testing in this environment offered a more rigorous test than in an open field. However, a few of the animal datasets were taken in rural agricultural fields to minimize the required human-animal interaction.

Figure 18 on the next page shows the mobile data collection platform built to facilitate the data collection process.



Figure 18. Mobile data collection platform (a) and close-up view (b).

As seen in Figure 18(b), the transmit and receive horn antennas on the radar cart are mounted to a metal plate for rigidity and can be manually rotated on-axis. The metal plate's machined preset rotation stops accommodate any combination of linear polarizations. The radar hardware is encased in a metal enclosure directly behind the antenna fixture. The digital camcorder to the left of the radar unit provides audiovisual documentation of each data file collected. The computer to the right of the radar hardware stores the large amount of data acquired from simultaneous acquisition of radar signatures and digital video. The monitor behind the computer provides a real-time display of target spectrogram signatures and radar parameters (target range, velocity, etc.). The mobile data collection platform transports easily to the testing location of choice.

## 7.2 Database Collection.

The goal to thoroughly study the micro-Doppler phenomenon required the collection of an expansive radar signature database. Well over 1,000 MFCW radar signatures were collected during the course of this project. In addition, over 300 basic CW radar signatures were acquired during earlier development stages.

The goal throughout the project was to obtain a wide variety of data files that represent operational conditions as much as possible. For example, targets approached the radar at numerous angles of approach, not simply directly toward the radar. Data files were also taken of targets roaming randomly in the radar range. The acquired data included three target classes: human, vehicle, and animal. Each target sub-dataset contains data from targets with varying speeds, approach angles, ranges, and postures. The human dataset includes files where the individual crawls toward the radar.

The animal dataset contains data from deer, dogs, and goats. The database also includes files with multiple targets of different classes simultaneously moving within the range of the radar.

### 7.3 Database Processing.

Figure 19 below illustrates the software processing steps prior to joint time-frequency detection for a 3FCW radar.

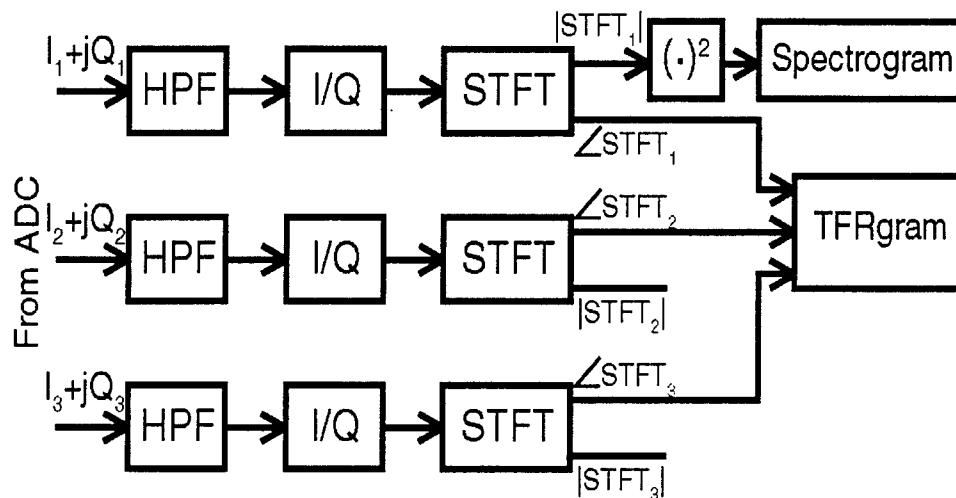


Figure 19. 3FCW radar processing prior to joint time-frequency detection.

For the MFCW radar, analog to digital conversion produces  $M$  complex baseband digital signals where  $M$  is the number of transmitted tones. A high-pass filter processes each complex channel to remove clutter and  $1/f$  noise around DC. The filter stopband must be narrow to minimize unwanted attenuation of target signal energy near DC.

The high-pass filter magnitude response is shown in Figure 20 below.

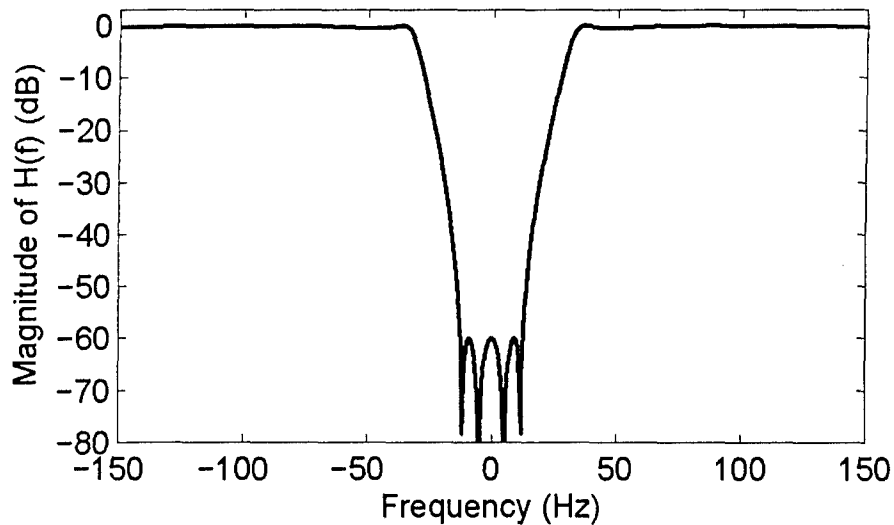


Figure 20. Magnitude of fourth-order elliptic high-pass filter transfer function.

The filter is a fourth-order elliptic high-pass filter with a 31.5Hz cutoff frequency, 60dB stopband attenuation, and 0.5dB ripple in the passband. The phase response is non-linear (the elliptic filter is IIR), but using the same filter on all complex channels maintains the proper phase difference between channels.

Following filtering, each inphase/quadrature signal pair undergoes I/Q error correction. I/Q error results from amplitude or phase imbalance in the quadrature demodulator and/or mismatched receiver channels following quadrature demodulation. I/Q error creates an “image target” in the spectrogram at the negative of the true target frequency. Providing that the image target is strong enough, a target tracking algorithm may report two targets present when there is actually only one. Figure 21(a) below shows a spectrogram of a human walking toward the radar and then turning around and walking away.

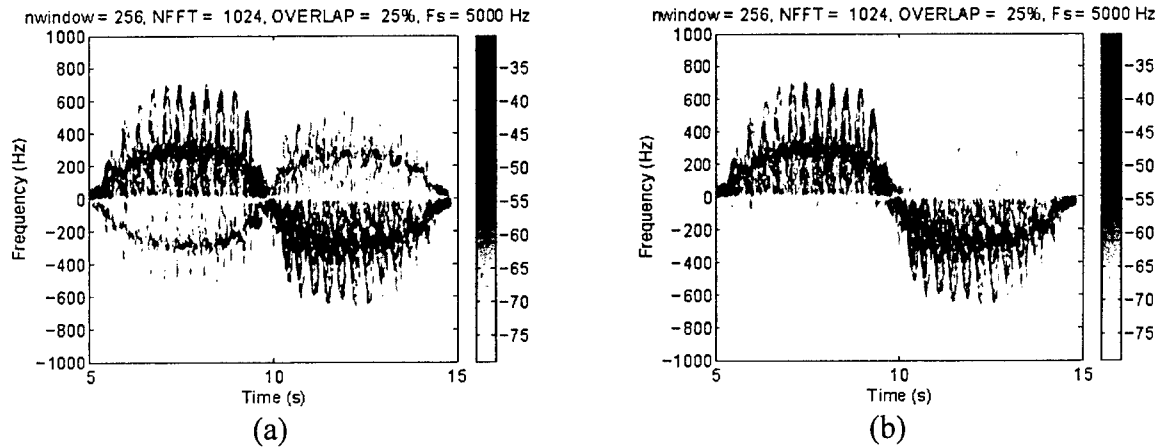


Figure 21. Spectrogram with strong image target (a) and corrected spectrogram (b)

An amplitude imbalance of 0.5mV and a phase imbalance of  $14^\circ$  produced an image target approximately 18dB below the true target power. Applying an I/Q error correction algorithm [13] reduced the image target power as seen in Figure 21(b).

After I/Q error correction, the Short-Time Fourier Transform (STFT) converts each complex channel into the joint time-frequency domain. The magnitude squared of one complex channel's STFT forms the spectrogram for target detection and tracking as developed in Section 5.3. The phase of the STFT of each channel is used to calculate the TFRgram as described in Section 5.4.

## Section 8

### Results from Ranging, Detection, and Micro-Doppler Feathre Evaluation

#### 8.1 Ranging Performance.

System specifications called for 1m (3.28ft) rms range accuracy (at the minimum required SNR of 13.5dB). To test the system's ranging performance, a person positioned at different ranges waved a trihedral corner reflector in one hand. The corner reflector provided a consistent target of known radar cross section. A laser range-finder with sub-inch accuracy positioned the person at a known range. Direct-conversion MFCW radars rely on target motion to obtain range data. Some error is introduced into the range accuracy calculation just by moving the target.

Figure 22 below displays the spectrogram and TFRgram of a person at 200ft waving a corner reflector in their left hand.

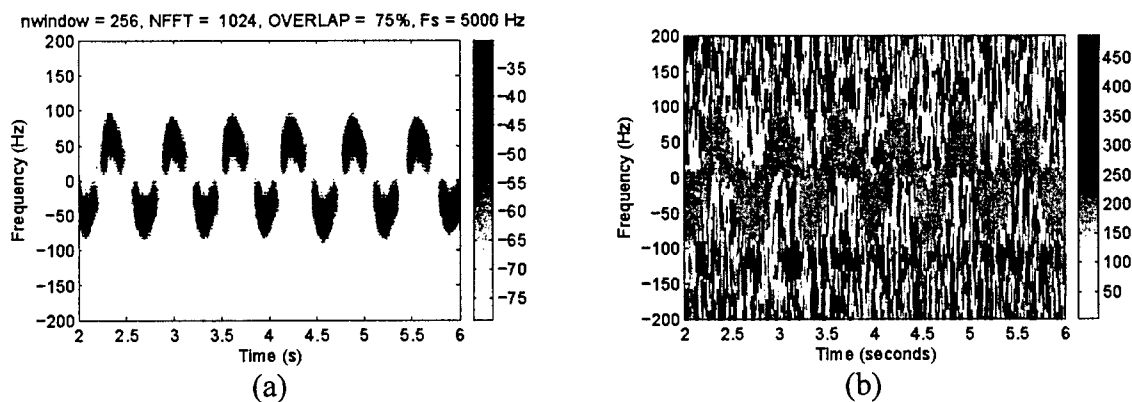


Figure 22. Spectrogram (a) and TFRgram (b) of corner reflector at 200ft

Using the methods of Section 5.5, the target range is extracted from the TFRgram. This calculation was performed for the radar's two frequency separations: 1MHz and 16MHz.

Example plots of range versus time for a corner reflector at 200ft are shown in Figure 23 below.

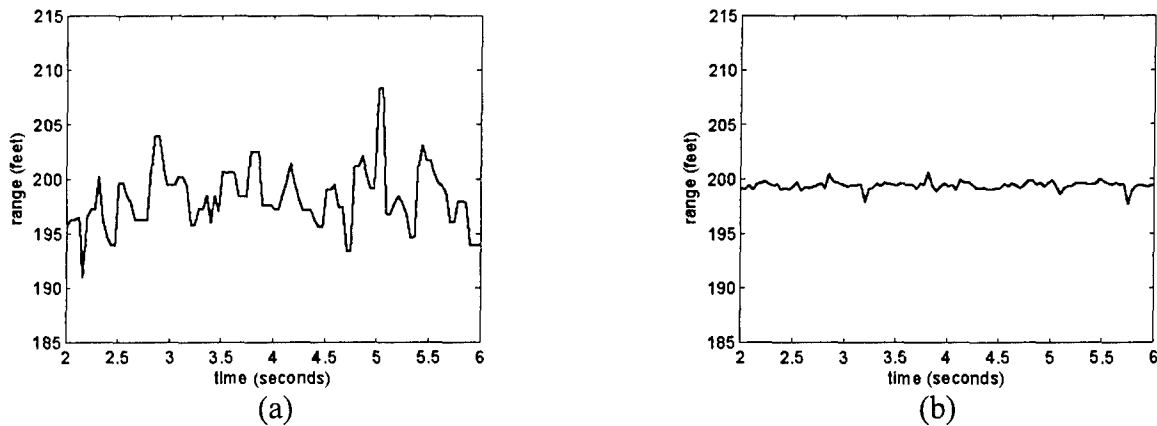


Figure 23. Corner reflector range results at 200ft with  $\Delta f = 1\text{MHz}$  (a) and  $16\text{MHz}$  (b)

The rms range accuracy for the corner reflector at 200ft range is 3.0ft for 1MHz frequency difference and 0.37ft for 16MHz frequency difference. The time-averaged range calculation is 198.1ft for 1MHz frequency separation and 199.3ft for 16MHz frequency separation. Table 7 below lists range calculations for different target ranges.

Table 7. Empirical range accuracy results.

Actual range	100ft	101ft	103ft	200ft	201ft	203ft
Mean range; 1MHz	99.1ft	102.3ft	104.6ft	198.1ft	199.6ft	200.9ft
Mean range; 16MHz	100.1ft	101.2ft	103.3ft	199.3ft	200.5ft	202.6ft
RMS accuracy; 1MHz	1.82ft	2.68ft	4.97ft	3.00ft	3.93ft	3.25ft
RMS accuracy; 16MHz	0.23ft	0.29ft	0.59ft	0.37ft	0.36ft	0.40ft

For 1MHz frequency separation, the rms range accuracy does not meet the 3.28ft system requirement for all the ranges listed. However, the radar achieves the requirement for 16MHz frequency separation. To compare the results, the theoretical rms range accuracy calculated from Equation (25) is 11.7ft for 1MHz frequency separation and 0.73ft for 16MHz frequency separation at 13.5dB SNR.

Figure 24 below plots range versus time for a human target jogging from 292ft to 15ft.

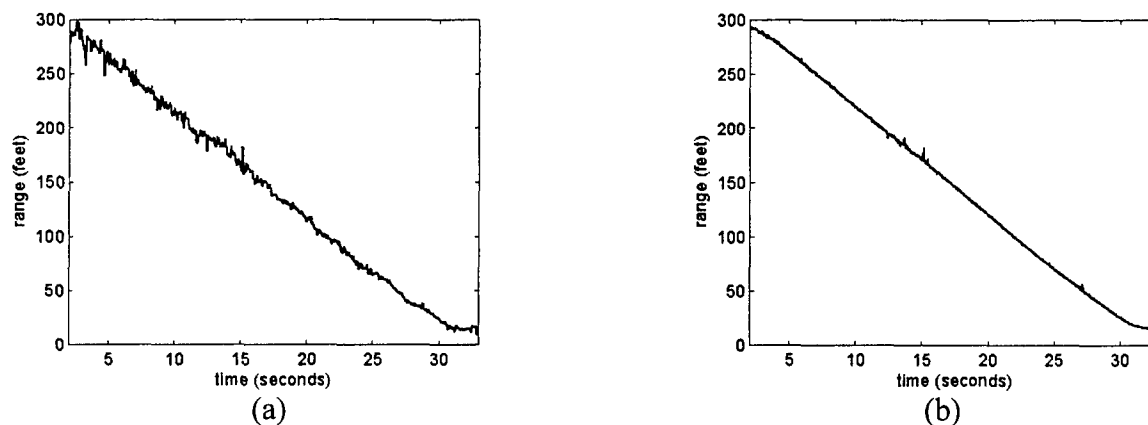


Figure 24. Range results for a human jogging from 292ft to 15ft with  $\Delta f = 1\text{MHz}$  (a) and 16MHz (b).

Changing from 1MHz to 16MHz frequency separation significantly improves the range results. A few moderate spikes still exist in the 16MHz range data. Most of these anomalies result from multipath signal loss or errors in target velocity tracking.

## 8.2 Detection Performance.

A rigorous analysis of a system's detection performance is often difficult to obtain for several reasons. Predicting performance under operational conditions adds additional complexity due to wide variations in target and noise statistics. Some of the difficulty arises due to RCS and multipath-induced signal fluctuation. The theory developed in Section 5 provides acceptable results for targets of constant or slowly varying amplitude. Both multipath and RCS variations often produce rapidly varying target amplitudes which result in brief periods of target loss. Another difficult task is calculating an accurate system false alarm rate. With average false alarm times specified in days, large amounts of data are required to determine the false alarm rate.

If automated methods of data collection are used, verifying a true false alarm also becomes challenging. We will focus on predicted maximum target range for a given (theoretical) probability of false alarm and detection and compare results to experimental data.

Using Equation (54), the predicted maximum range for various targets is tabulated in Table 8 below.

Table 8. Maximum detectable target ranges for  $P_d = 0.9$  and  $P_{fa} = 3.3 \times 10^{-7}$ .

Target	Average RCS	Maximum detectable range
Human	$0.75\text{m}^2$	73.8m (242ft)
Vehicle	$10\text{m}^2$	141m (463ft)
Animal	$0.1\text{m}^2$	44.5m (146ft)

Table 8 reveals that both human and vehicle targets meet the maximum detectable range requirements while animals do not. The small radar cross section of many animals causes reduced detection range. Note that Table 8 uses a single value for the RCS of each target class. The RCS values in Table 8 are fairly good approximations for the targets of interest to this project. However, the results of Table 8 would vary dramatically if (for example) the RCS of an elephant was used for the animal class.

Let us compare the predicted results of Table 8 to the results from experimental data. As discussed in Section 5.3, we define a *system-level* detection as an event when two or more *pixel* detections occur within a single FFT. We seek the empirical maximum detectable range to a target for a specified system-level probability of false alarm and detection. We use the approximation to the maximum detectable range that follows. If, for example, the time between spectrogram FFTs is 38.5ms, the number of FFTs per second is approximately 26. For a one second observation period and a probability of system-level detection of 0.9, the average number of missed detections is approximately three at the maximum detectable range ( $26 \times 0.1 \times 1 = 2.6 \approx 3$ ). The maximum detectable range is then the shortest range where the number of missed detections over a one second interval is three or more.

More generally, for an FFT time interval and a system-level probability of detection

$T_{FFT} P_{d,sys}$

$$N_{miss} \approx \left\lceil \frac{1}{T_{FFT}} (1 - P_{d,sys}) \Delta t \right\rceil \quad (62)$$

where  $\lceil \cdot \rceil$  is the ceiling operation and  $N_{miss}$  is the average number of missed detections over the interval  $\Delta t$ .

Figure 25 on the next page shows the spectrogram of a human jogging from 292ft to 15ft before and after detection (see Figure 24 for the range). We note that in the post-detection spectrogram, system-level detections (two or more detections per FFT) are achieved out to 292ft. However, there are many time intervals where no system-level detections occur.

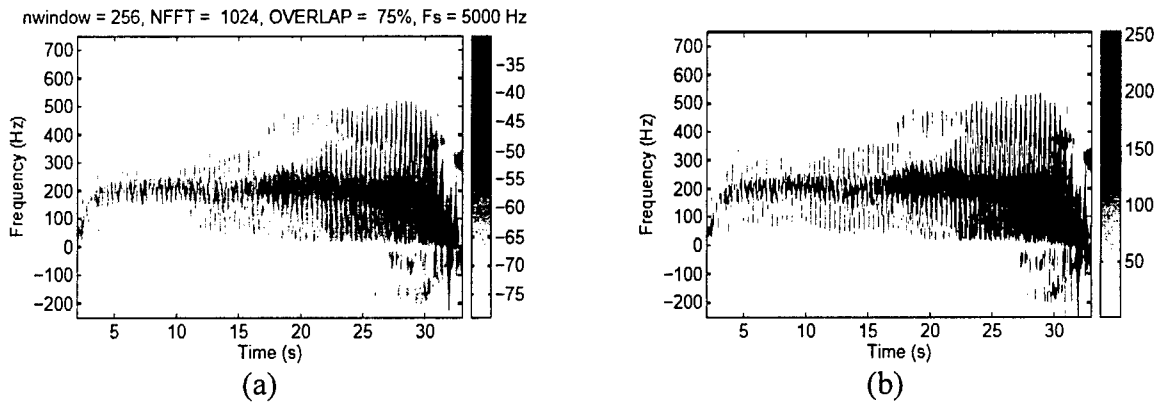


Figure 25. Spectrogram of jogging human before (a) and after (b) detection

The number of detections per FFT from Figure 25 is calculated and displayed in Figure 26 (a) below. Figure 26 (b) plots the received power versus time for the jogging human.

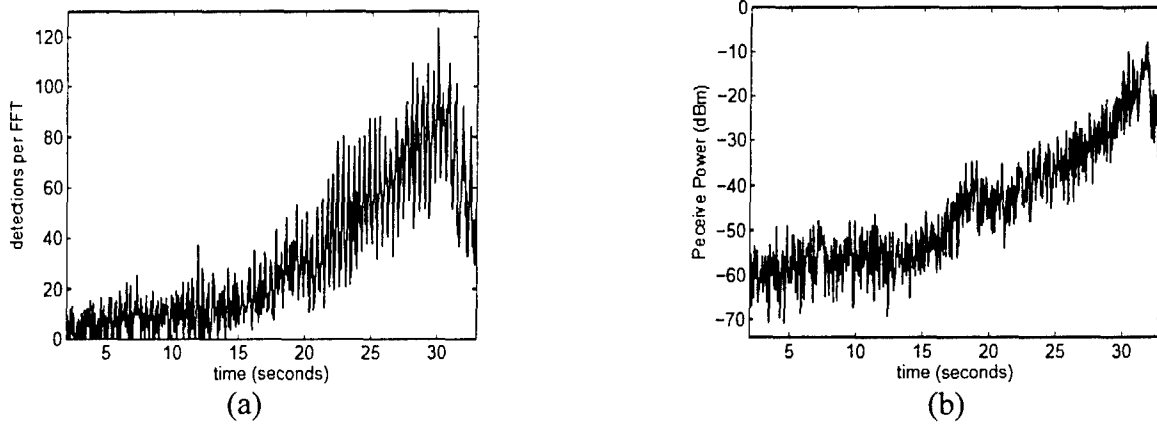


Figure 26. Number of detections per FFT (a) and received power (b) for jogging human.

The fast, deep signal fades that occur in typical datasets are readily seen. These signal fades result in higher numbers of missed detections in regions of low SNR.

Analysis of the data of Figure 26 (a) results in three missed detections per second occurring around 8.7 seconds. Consulting Figure 24(b), the target's range at 8.7 seconds was 232.8ft. Thus, the approximate maximum detectable range for this target is 232.8ft. The results of further detection range testing are listed in Table 9 below.

Table 9. Empirical maximum detectable range.

Target Class	Average maximum detectable range	# of files averaged
Human	66.5m (218.3ft)	5
Vehicle	105.2m (345.1ft)	5
Animal	40.1m (131.6ft)	5

Five files in each target grouping were averaged to obtain these results. Comparing Table 9 to Table 8, we see that the empirical maximum ranges were less than the predicted maximum ranges in all target classes. A primary cause of this discrepancy is the deep signal fading shown in Figure 26(b).

### 8.3 Spectrograms of Various Targets.

Figure 27 on the next page shows spectrograms of a human target running, jogging, and walking from a range of 150ft to 100ft and then back to 150ft.

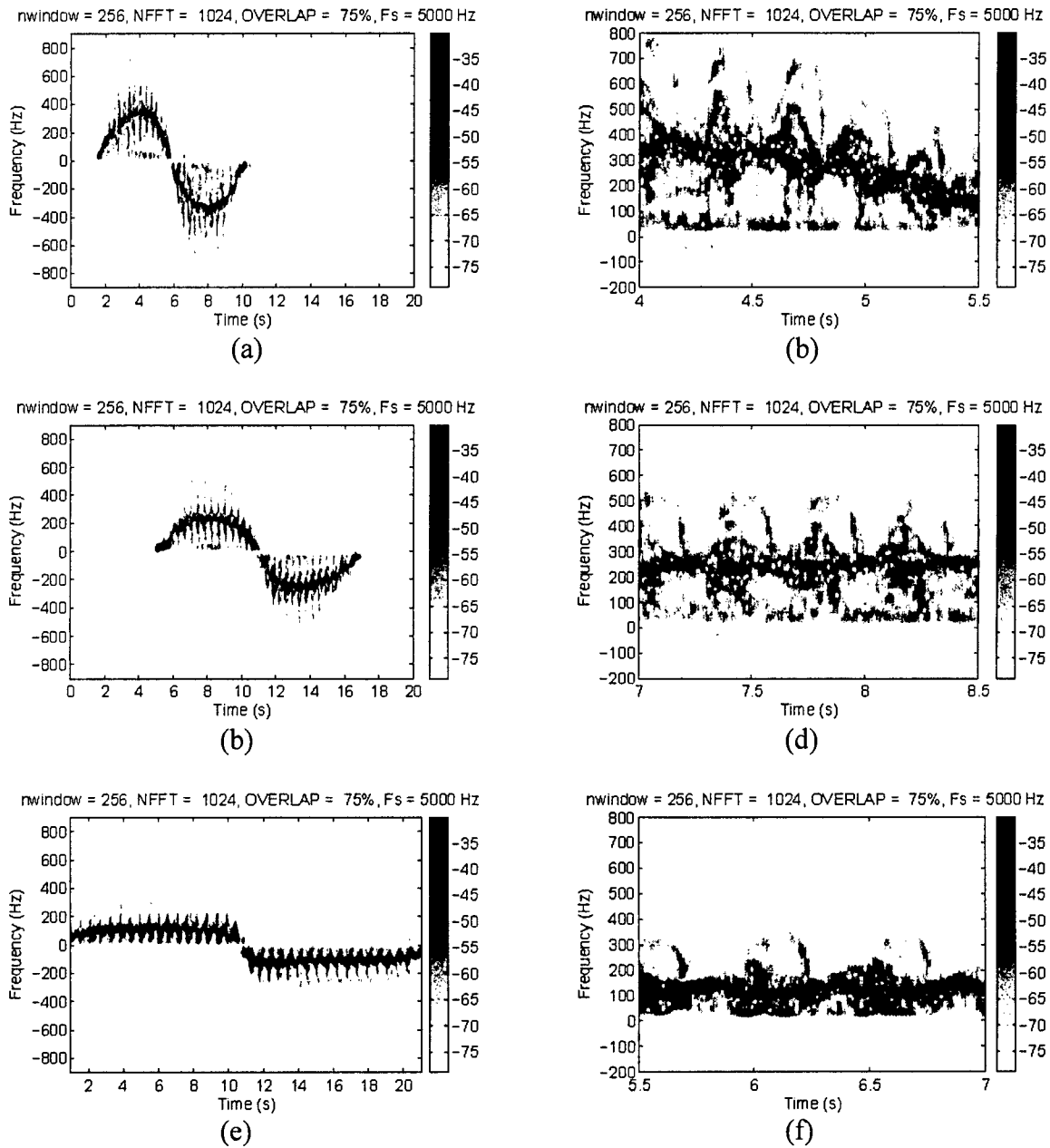


Figure 27. Spectrogram of human running (a), jogging (c), and walking (d). Expanded views are (b), (d), and (f), respectively.

Figure 27 (a), (c), and (e) reveal the coarse differences in micro-Doppler over varying target speed. As expected, maximum micro-Doppler frequency and legswing rate increase as the target reaches faster speeds. The expanded views in Figure 27 (b), (d), and (f) expose fine micro-Doppler features. Returns from all target scattering centers that move at nearly the same speed as the torso, “torso returns,” appear as the darkened line running through the spectrograms. The large arches over the torso return result from legswing motion. When one leg is planted on the ground (foot not moving relative to the radar), that leg’s return appears at DC [3]. Armswing can be seen as the smaller arches around the torso return. As seen in Figure 27 (b), (d), and (f), the armswing becomes more pronounced with higher speed.

The targets in Figure 27 all move along a radial path from the radar that is centered on the radar antennas. This zero degree approach angle makes the relative velocity calculated from the Doppler return (approximately) the true target velocity. Data files were acquired from targets moving at various approach angles to observe its effect on the radar signatures. Figure 28(a) below shows the spectrogram of a human walking at a 45° approach angle from a range of about 100ft to 50ft.

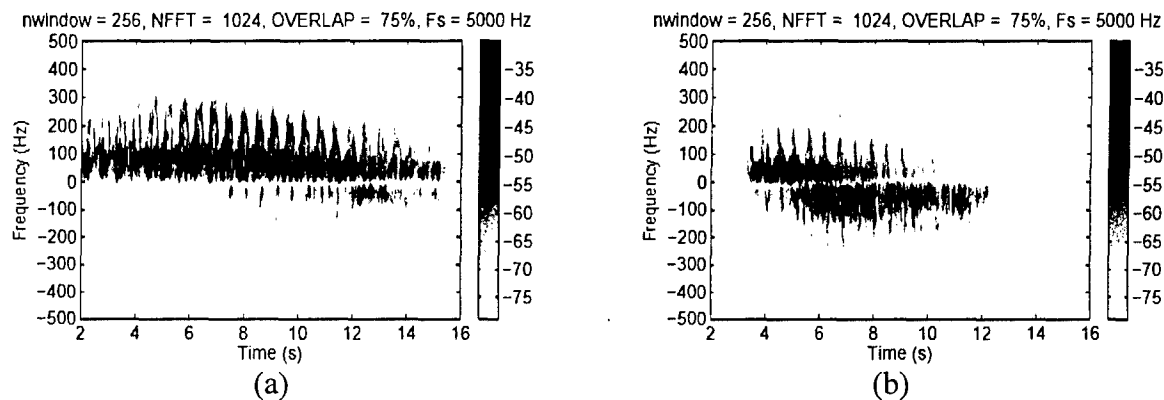


Figure 28. Human target walking at 45° (a) and 90° (b) relative to radar.

The spectrogram of a target approaching at 45° does not drastically differ from that of a target approaching at 0°. However, the received signal strength appears to drop off near the end of the file, even though the target is approaching the radar. This effect is explained by the fact that the target is passing through the antenna beamwidth. Figure 28(b) shows a human walking at (approximately) a 90° angle relative to the radar at 50ft range. The radar still receives a strong return from the target, but the spectrogram looks quite different from the 0° approach angle case. The target signature is now centered on DC and the returns from leg and arm motion extend in both positive and negative frequency directions. In addition, the leg and arm returns are of much shorter time duration.

Crawling human targets illustrate the effects of varying posture on target signatures. Figure 29 (a) below shows a human crawling toward the radar from a range of 100ft to 85ft.

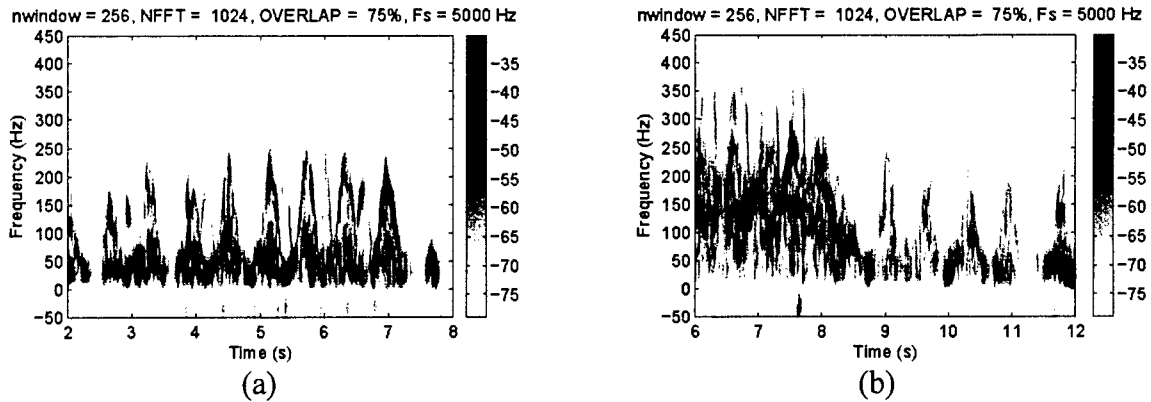


Figure 29. Human crawling (a). Transition from walking to crawling (b).

The crawling target's torso return concentrates close to DC. In contrast to a walking human, the crawler's micro-Doppler energy from leg and arm motion is highly skewed to one side of the torso return. In addition, the period between micro-Doppler peaks from the limbs is typically longer for a crawler than for a walker. This effect is illustrated in Figure 29 (b) which shows a human transitioning from walking to crawling.

In addition to humans, data was collected from vehicular targets. Most of the vehicle data came from either a Jeep Cherokee or a Ford Taurus station wagon, but random passing vehicles also became part of the datasets. Major differences exist between human and automobile Doppler signatures. As seen in Figure 30 below, a typical automobile radar signature is strongly concentrated on a single line in the time-frequency plane. Figure 30 displays the spectrograms of an automobile driving from a range of 250ft to 100ft with various accelerations and velocities.

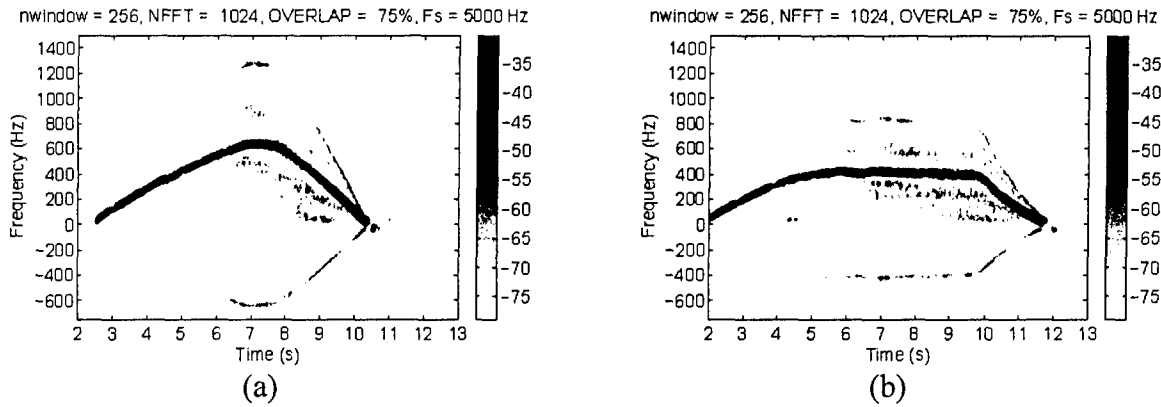


Figure 30. Vehicle driving at different velocities and accelerations.

Most vehicles contain several predominant scattering centers, but all of these scattering sites move at roughly the same speed relative to the radar. A notable exception is a helicopter where the rotor blades cause large sinusoidal micro-Doppler around the helicopter body return [14]. Since most automobiles are rigid scatterers, one would not expect to see (in theory) the Doppler returns in Figure 30(a) other than the main return. An image signal can be seen at the negative frequency of the main return. This signal is not a physical phenomenon of the target but an artifact of receiver inphase/quadrature error (as discussed in Section 7.3). An I/Q error correction algorithm was applied to this data, but complete error correction was not achieved. In addition to the I/Q error signal, another artifact signal occurs at twice the frequency of the main return. This artifact signal results from harmonic distortion in the receiver at high input signal levels. Figure 30(a) also contains artifacts from the phase noise of the local oscillators. Phase noise artifacts can be seen close-in on either side of the main return. Artifact signals are present in human data also, but the signal strength of vehicular targets raise the artifact signal levels well above the system noise floor.

As with the human targets, the vehicles' approach angle was varied to observe its effect on the Doppler signatures. Figure 31(a) below shows the spectrogram of a vehicle driving from a range of 250ft to 150ft at an angle of approximately 45°.

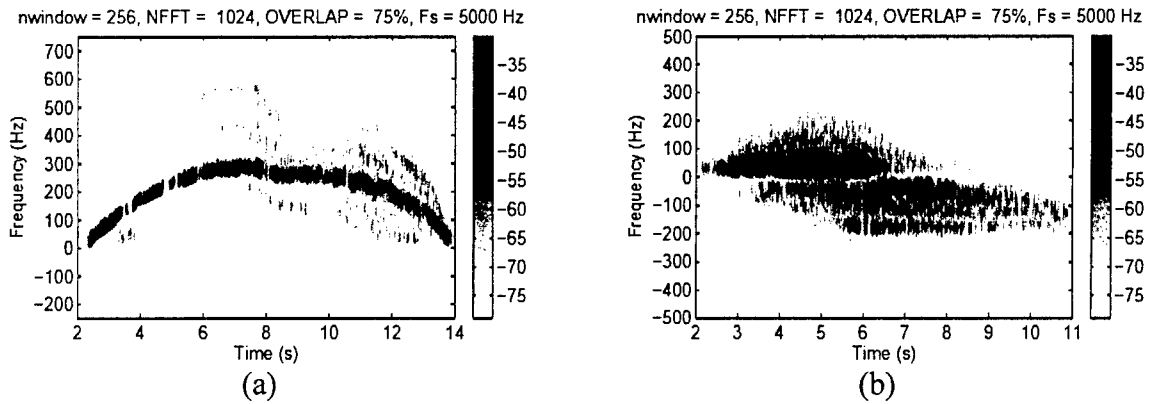


Figure 31. Vehicle driving at 45° (a) and 90° (b) relative to radar.

The vehicle's Doppler signature does not change significantly by varying the approach angle from 0° to 45°. However, when the approach angle is approximately 90° the vehicle Doppler signature differs markedly as seen in Figure 31(b). The primary difference is that the main return energy is spread out much more in frequency for the 90° approach angle case. Comparing Figure 31(b) to Figure 28(b), we see that at a 90° approach angle, distinguishing between vehicle and human spectrograms becomes more difficult.

Figure 32 on the next page displays an interesting spectrogram of a vehicle turning a corner at close range to the radar.

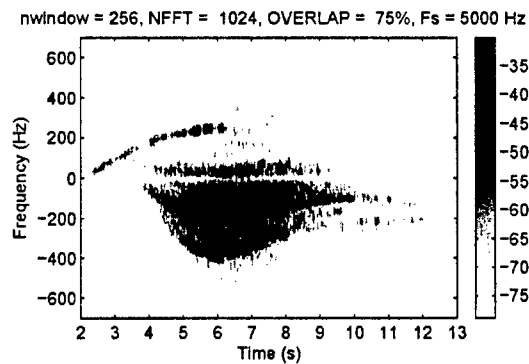


Figure 32. Vehicle turning in front of radar at close range.

Referring back to Figure 17, the vehicle begins by driving behind and to the left of the radar unit. The vehicle then takes a right turn in front of the radar and continues to drive until the vehicle is well beyond the antenna beamwidth. One interesting feature of Figure 32 is the positive frequency return that starts at around 2 seconds and ends at 6 seconds. This return is not an artifact but a multipath return from the building in the upper right-hand corner of Figure 17. The multipath return shows up almost 2 seconds before the main return, and a tracking algorithm would likely report the multipath signal as another target.

Figure 33 on the next page shows the spectrogram of a vehicle driving toward the radar at a  $0^\circ$  approach angle and coming to a complete stop 50ft in front of the radar.

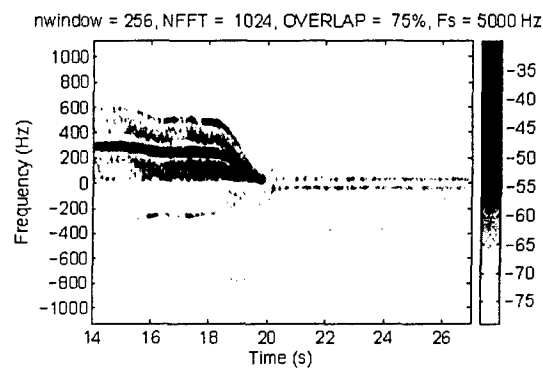


Figure 33. Micro-Doppler produced by engine is visible at close range

Although the vehicle is at a complete stop, the spectrogram contains numerous micro-Doppler lines. A combination of vibrating and rotating parts in the vehicle's idling engine produce the various micro-Doppler features of Figure 33.

In addition to humans and vehicles, the micro-Doppler features of animals were also studied. The animal datasets included dog, goat, and deer. Figure 34 on the next page displays spectrograms from each animal type.

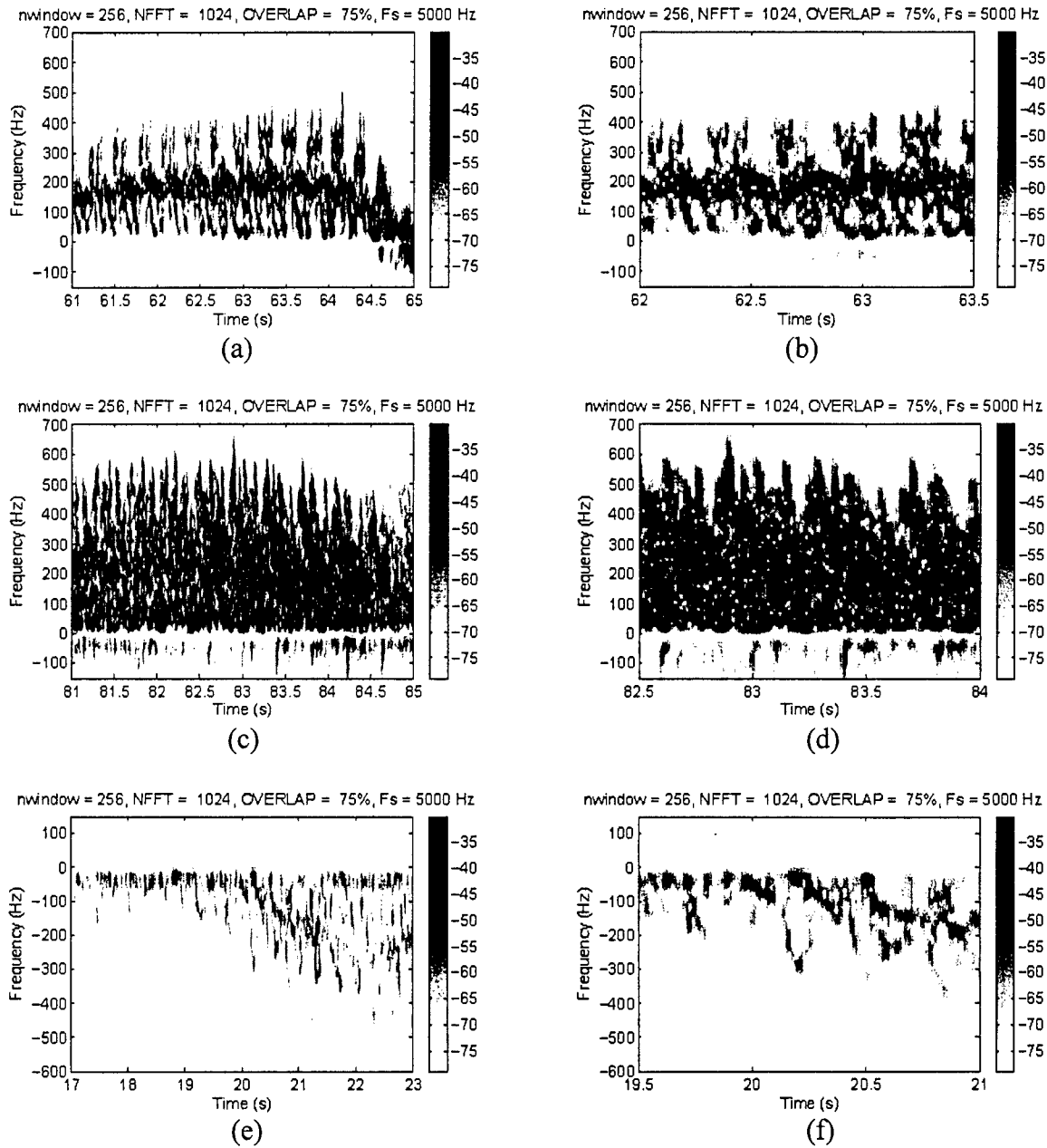


Figure 34. Spectrogram of dog (a), goat (c), and deer (d). Expanded views are (b), (d), and (f), respectively.

A dog approaching the radar produced the spectrogram of Figure 34 (a). Approximately four goats running toward the radar contributed to the Doppler signature of Figure 34 (c). In Figure 34 (e), a deer casually wanders around until it leaps into the air and bolts off after being startled.

Animal leg motion produces micro-Doppler of short time duration compared to a human approaching the radar at the same speed.

This effect is due to the observation that most quadruped animals' stride rate is considerably faster than for biped animals. The overall micro-Doppler signature due to dogs and goats appears fairly similar. The deer micro-Doppler (other than a faster stride rate) closely resembles the micro-Doppler of a crawling human as seen in Figure 29. Before the deer bolts off, the main return from the deer is near DC, with the leg micro-Doppler skewed to one side, similar to the return from a crawling human.

All of the previously displayed datasets contain only one target in each data file. Numerous data files were collected with multiple targets in motion at the same time. Two examples of multi-target data files are shown in Figure 35 below.

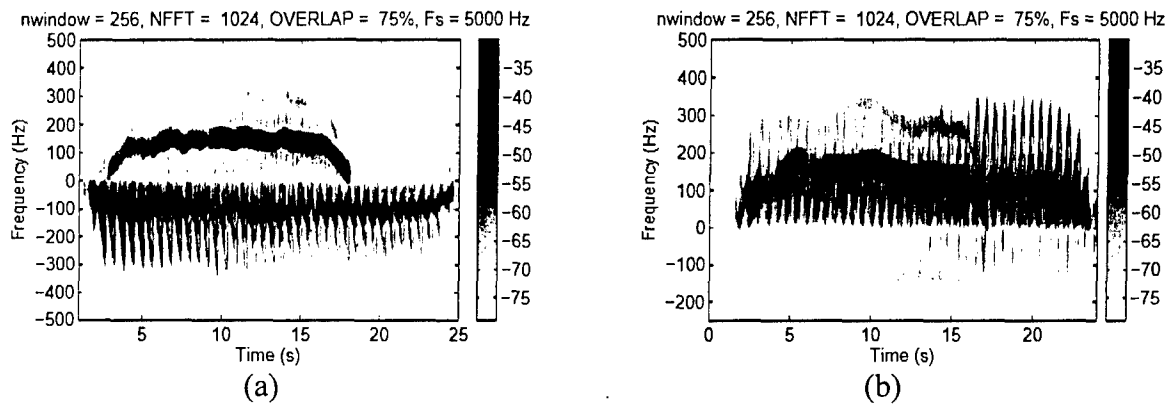


Figure 35. Multiple targets moving in opposite directions (a) and the same direction (b).

Figure 35 (a) displays the spectrogram of a vehicle driving from 250ft to 150ft while a human walks from 50ft to 150ft. With the targets moving in opposite directions, little Doppler overlap occurs. The individual targets can be isolated by their Doppler separation only. In Figure 35 (b), a human walks from 150ft to 50ft while a vehicle drives from 250ft to 150ft. Since the two targets move in the same direction and at roughly the same speed, significant Doppler overlap occurs. Some target separation could be achieved through range tracking.

A limited amount of data was acquired during adverse weather conditions. The spectrogram of ambient conditions during heavy rain appears in Figure 36(a) below.

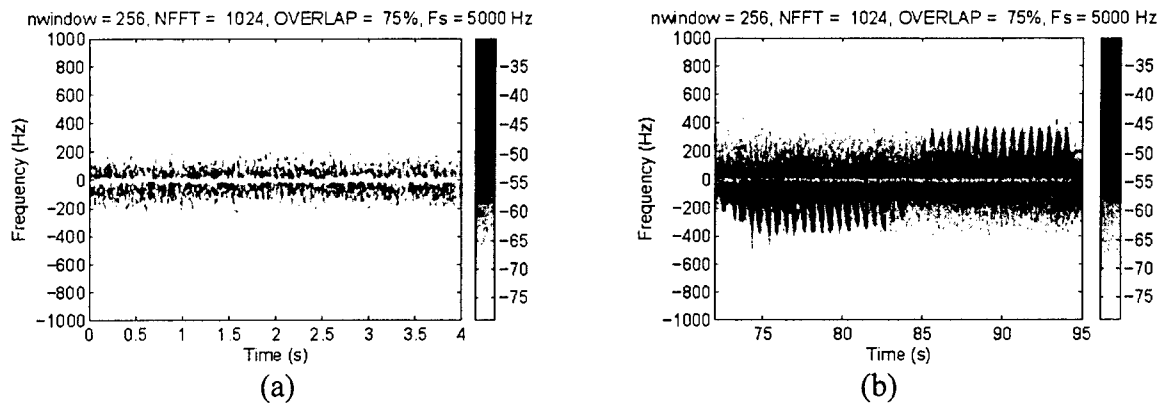


Figure 36. Spectrogram of ambient conditions (a) and human target (b) during heavy rain.

A significant clutter region forms around DC due to the rainfall. The rest of the spectrogram is relatively unaffected by the rain. Figure 36 (b) shows a human walking away from and then toward the radar during heavy rain. The target is still easy to detect visually, but a fixed-threshold automatic detection algorithm would likely report a high number of false alarms due to the rain. Further study of this issue and an investigation into the use of Constant False Alarm Rate (CFAR) detectors is planned.

#### 8.4 Radar Cost Analysis.

The system cost specification requires a per-unit cost of under \$1,000. This cost point demanded significant design tradeoffs. For example, a single X-band power amplifier packaged in a shielded box with moderate performance can cost over \$2,000. To reduce cost, a surface-mount power amplifier was chosen (with lower gain and output power) that costs under \$30 per unit in small quantities.

Table 10 below lists the costs of various components of the radar design for small production quantities.

Table 10. Small quantity radar cost analysis.

Cost Category	Aggregate Cost
Receiver front-end devices	\$410
Cables and connectors	\$100
Antennas	\$40
Waveguide to coax converters	\$200
Shielded chassis	\$70
Microwave PCB fabrication	\$180
Baseband PCB fabrication	\$80
Baseband components	\$165
Total	\$1,245

Table 10 includes the cost of adding Digital Signal Processor (DSP) hardware to perform the radar calculations instead of the personal computer currently being used. The radar cost of \$1,245 nearly reaches the specified goal of less than \$1,000 per unit even in small quantity production. The specified price point will likely be achieved for moderate to large production quantities. If a lower cost for small quantity production is desired, further design refinements can be made.

## Section 9 Theory and Design of Target Classification Systems

### 9.1 Introduction.

Classification is the process of separating objects into groups by comparing their attributes. The human body is an example of a complex classification system. Our eyes, skin, tongue, ears and nose constantly deliver raw information to our brains about the world around us. The brain is tasked with sorting through all of the raw signals and extracting important features for a given classification task. For example, while driving our brains use our sense of sight to estimate the size and shape (among other features) of road obstacles. If a child were to walk into the middle of the road, the brain would use the extracted features to (hopefully) classify the object in the road as a child and stop the vehicle. The massive parallelism of the brain allows us to perform complex classification tasks with ease.

Due to the ability of the human brain to excel at classification under widely varying conditions, many classification systems today still incorporate a human operator at some point in the system. In fully-automatic classification systems, a computer performs all steps of the classification procedure with no assistance from a human operator. This project involves the design of a fully-automatic target classifier. Figure 37 on the next page illustrates the procedural block diagram of a typical classification system.

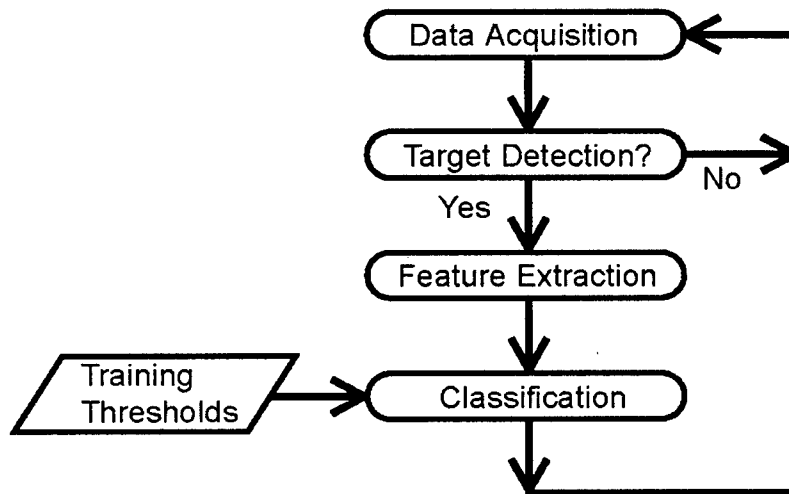


Figure 37. Block diagram of a typical real-time classification system.

The classification procedure begins with the acquisition of a frame of raw data. The data are then fed into a target detection algorithm. If the detection algorithm decides that a target is present, the target features are extracted from the data. In the feature extraction stage, the data frame is processed to quantify the various target features used for classification. The classification stage then compares the extracted feature values to thresholds previously determined by a training procedure. The classification step produces the estimated target class, and then the cycle repeats for subsequent data frames.

Data acquisition and target detection were discussed in earlier sections of this report. Feature extraction, classifier training, and classification stages will be the topics of the remainder of this section.

## 9.2 Feature Extraction.

Feature extraction begins with the estimation of basic target parameters such as received signal power, range, and velocity. The received signal power is calculated simply by extracting the target power from the spectrogram using the velocity estimate (and scaling by the receiver gain). Section 5.5 of this report developed target range and velocity estimation as applied to this project. Target features used for classification are derived from the basic target parameters. Estimates of a target's radar cross section, "normalized bandwidth," and legswing period provide the basis for this project's target recognition algorithm.

The Radar Cross Section (RCS) can be roughly thought of as the ratio of scattered power (per unit solid angle) to incident power density. The mathematical definition of RCS is

$$\sigma \triangleq \lim_{R \rightarrow \infty} 4\pi R^2 \left| \frac{E_r}{E_i} \right|^2 \quad (63)$$

where  $\sigma$  is the RCS,  $R$  is the range to the target,  $E_r$  is the reflected field strength, and  $E_i$  is the incident field strength. In practice, the limit in Equation (63) means that a target's RCS should be measured in the far-field region of the radar. The RCS is a random variable that depends on frequency, aspect angle, antenna polarization, target geometry, and target material. The random nature of RCS causes fluctuations in target signal strength that often significantly affect the detection process.

Although random, an estimate of radar cross section is a natural feature for target classification. Small targets tend to have smaller RCS values on average than larger targets.

Equation (28) in terms of received power is

$$R = \left[ \frac{G_t G_r P_t \lambda^2 \sigma}{(4\pi)^3 P_r L} \right]^{1/4} \quad (64)$$

where  $P_r$  is the received signal power referenced to the receiver input. Solving for  $\sigma$  yields the RCS estimate

$$\hat{\sigma} = \frac{(4\pi)^3 R^4 P_r L}{G_t G_r \lambda^2 P_t} \quad (65)$$

After designing the radar, the variables  $L$ ,  $G_t$ ,  $G_r$ ,  $\lambda$ , and  $P_t$  become (approximately) constants. The only remaining variables in Equation (65) are the target range and the received signal power. An important fact to note is that Equation (65) neglects the effects of multipath on the RCS estimate. To counteract the effects of multipath, the RCS estimate is averaged over the detection frame.

A target's radar cross section alone does not provide robust target classification. Another target feature we will refer to as the "normalized bandwidth" further aids classification. The first step in calculating the normalized bandwidth is to estimate instantaneous bandwidth. Figure 38 below illustrates the instantaneous bandwidth.

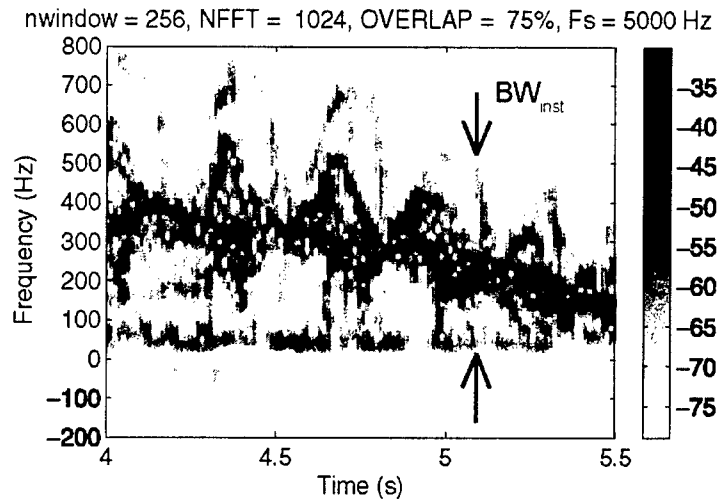


Figure 38. Instantaneous bandwidth.

The instantaneous bandwidth essentially calculates the frequency width of the target spectrogram at each time instant. Normalizing the instantaneous bandwidth by the total frequency width of the detection frame and dividing out the target speed determines the normalized bandwidth.

$$BW_{norm} = \frac{BW_{inst} / \Delta f_{frame}}{speed + 1} \quad (66)$$

where  $\Delta f_{frame}$  is the frequency width of the detection frame,  $BW_{inst}$  is the instantaneous bandwidth,  $speed$  is the magnitude of the target velocity. Please note that the units of  $speed$  are not frequency units. The normalized bandwidth feature helps distinguish between humans and vehicles since the frequency spread of a human target is typically much larger than that of a vehicle.  $BW_{norm} \cdot speed \cdot BW_{norm}$

Although RCS and normalized bandwidth are good classification features, the legswing period feature is required to reliably distinguish crawling humans from animals. Calculating the legswing period begins by accumulating the target energy above (or below, depending on the direction of motion) the average target velocity

$$x[n] = \sum_{k > k_{avg}} |STFT[k, n]|^2 \quad (67)$$

where  $k_{avg}$  is the frequency bin of the average target velocity, and  $\sum_{k > k_{avg}} |STFT[k, n]|^2$  is the accumulated target energy. The discrete autocovariance function  $c_{xx}(\tau)$  provides a measure of the periodicity of a discrete-time sequence  $x[n]$ . The autocovariance function is defined as

$$c_{xx}(\tau) = \frac{1}{M} \sum_{i=1}^{M-\tau} (x[i] - \bar{x})(x[i+\tau] - \bar{x}) \quad \text{where } \bar{x} = \frac{1}{M} \sum_{i=1}^M x[i] \text{ and } \tau = 0, 1, \dots, M \quad (68)$$

where  $M$  is the number of samples in  $x[n]$  and  $\tau$  is the lag variable. The autocovariance function is typically normalized so that the autocovariance at zero lag is equal to unity. Peaks in the autocovariance function reveal periodicities in the input sequence. The legswing period estimate is then the time difference between the peak at zero lag and the next closest peak of  $T_{leg} c_{xx}(\tau)$ . Figure 39 on the next page shows calculation of the legswing period for a human target.

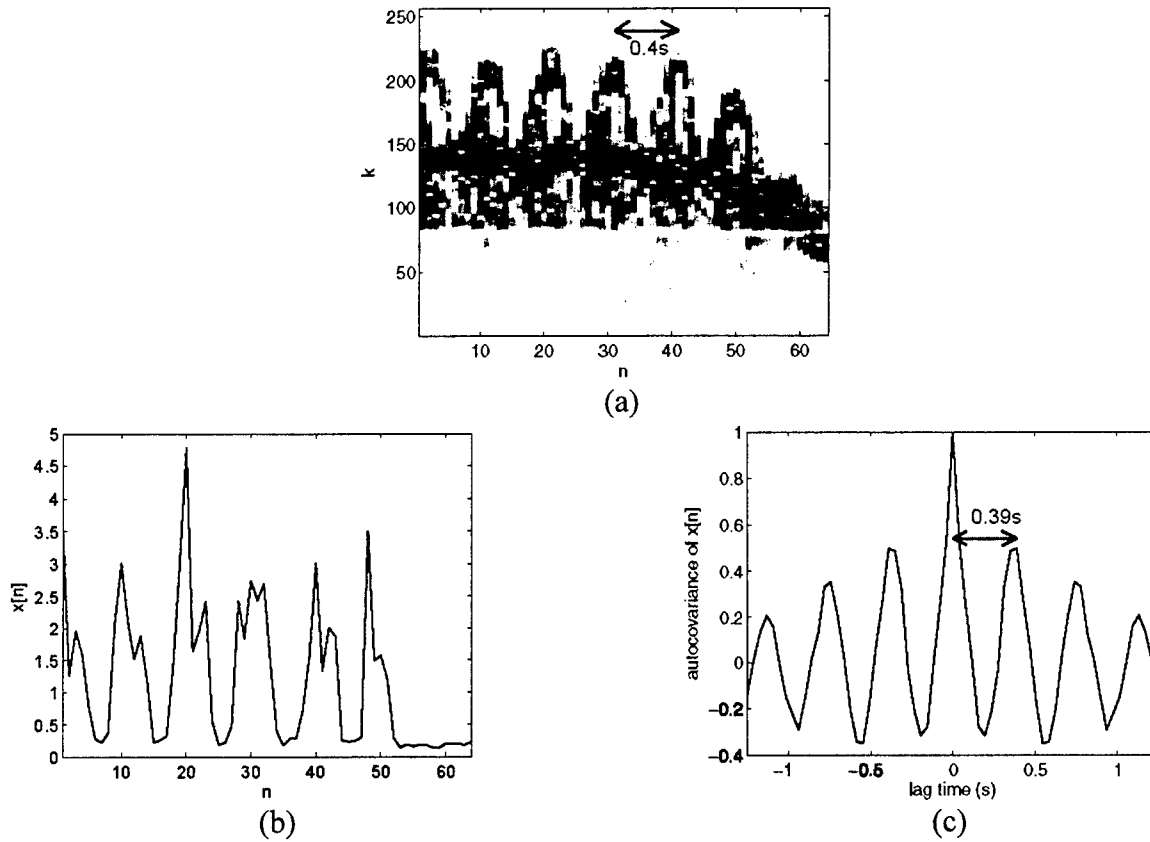


Figure 39. Calculating legswing period: spectrogram (a),  $x[n]$  (b), and autocovariance (c).

We see in Figure 39 that the autocovariance provides a good estimate of average legswing period.

### 9.3 Feature Space.

To develop the geometric interpretation of target classification, we begin by introducing the *feature vector*. The feature vector groups  $M$  target features into an  $M$ -dimensional vector  $\vec{x}$ . The  $M$ -dimensional space created by  $\vec{x}$  is called *feature space*. Each frame of data gets mapped into a single point in feature space. This work uses three target features, so feature space is three-dimensional.

The feature vector is structured as

$$\vec{x} = \begin{bmatrix} \sigma \\ BW_{norm} \\ T_{leg} \end{bmatrix} \quad (69)$$

Figure 40 below displays the first two dimensions of feature space with test data from humans, vehicles, and animals.

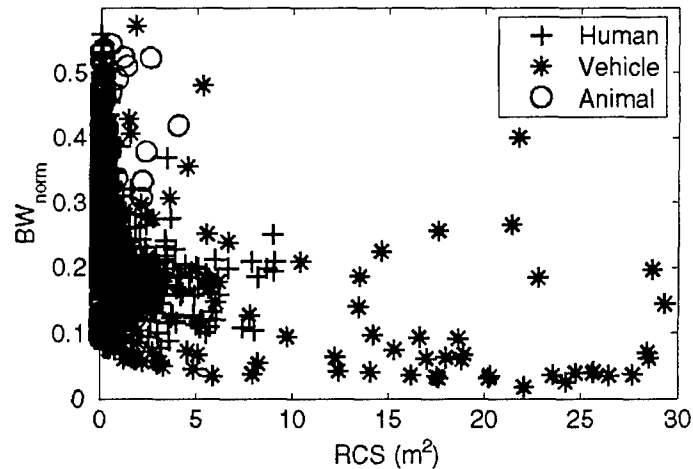


Figure 40. Two-dimensional view of feature space (testing set).

As expected, most of the vehicle data frames are located at high RCS values while the animal data frames are concentrated in regions of low RCS. In only two dimensions, significant overlap occurs between the classes. The legswing period feature further separates the classes.

#### 9.4 Classifier Training and Testing.

In order to calculate decision regions (regions of feature space assigned to a certain class), one must first separate the experimental database into a *training set* and a *testing set*. The training set is used to calculate the decision regions. The testing set uses the decision regions to evaluate the performance of the classifier.

The sequence performed to train the classifier is illustrated in Figure 41 below.

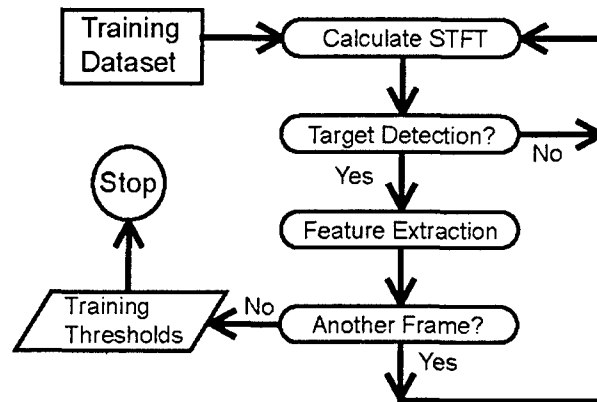


Figure 41. Offline training sequence.

The offline training sequence extracts features from all of the files in the training dataset. The decision regions are then calculated from the feature space of training data frames. Figure 42 below illustrates the offline testing sequence.

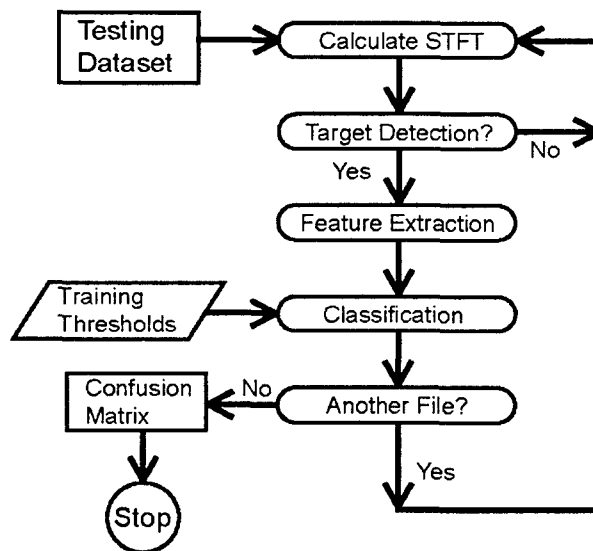


Figure 42. Offline testing sequence.

The testing sequence classifies each data file in the testing dataset using the decision regions calculated from the training set. The testing set is labeled with the correct classification for each file. The estimated target class is then compared to the true target class. The overall performance of the classifier is quantified in the confusion matrix which is the subject of the next section.

### 9.5 Quantifying Classifier Performance With Confusion Matrices.

Confusion matrices are often used to evaluate the performance of classifiers. We will motivate the use of confusion matrices by a few straightforward examples. Consider the scenario of a worker sorting produce on an assembly line. Two types of fruit pass along the assembly line: apples and oranges. The worker's goal is to throw away (alarm on) all apples while leaving all oranges on the assembly line. The plant manager decides to test the worker's performance. A total of 10 apples and 15 oranges are placed on the assembly line. The worker sorts the fruit and then the plant manager evaluates the worker's performance with a confusion matrix. The results of the test are shown in Table 11 below.

Table 11. Two-class confusion matrix.

Actual Class		Chosen Class	
		Apple	Orange
Apple	7	3	
Orange	2	13	

In the first row and first column of numbers, we see that when the *actual* piece of fruit on the assembly line was an apple, the worker correctly *chose* an apple 7 times. In the first row and second column, when the actual piece of fruit on the assembly line was an apple, the worker incorrectly chose an apple 3 times. Moving on to the second row and first column, when the actual piece of fruit on the assembly line was an orange, the worker incorrectly chose an apple 2 times. Finally, when the actual piece of fruit on the assembly line was an orange, the worker correctly chose an orange 13 times. The correct classification decisions are along the diagonal of the matrix.

Since there are only two classes in this problem, we can calculate a probability of detection and false-alarm for classification. We consider a classification detection as an event when the worker (correctly) throws away an apple when an apple is present. The probability of classification detection is then

$$P_{d,class} = \frac{\# \text{ of apples chosen as apples}}{\text{total \# of apples}} = \frac{7}{7+3} = 0.70 \quad (70)$$

A classification false alarm occurs when the worker (incorrectly) throws away an orange. The probability of classification false alarm becomes

$$P_{fa,class} = \frac{\# \text{ of oranges chosen as apples}}{\text{total \# of oranges}} = \frac{2}{2+13} = 0.13 \quad (71)$$

Now suppose the test is repeated with the same number of apples and oranges, except now 20 bananas are placed on the assembly line. The worker must now sort the fruit into three separate bins for each type of fruit. Since this is a three class problem, the confusion matrix becomes a 3x3 matrix. Table 12 on the next page shows the worker's performance in this task.

Table 12. Three-class confusion matrix.

		Chosen Class		
		Apples	Oranges	Bananas
Actual Class	Apples	6	3	1
	Oranges	1	12	2
	Bananas	2	3	15

Since this is a three-class problem, simple probabilities of detection and false alarm cannot be determined (unless two classes are grouped together as one). Two common performance measures are average percent correct and accuracy. The percent correct per class is calculated for each class and then averaged.

The average percent correct is then

$$\overline{PC} = \frac{(PC_{apples}) + (PC_{oranges}) + (PC_{bananas})}{3} \quad (72)$$

where  $\overline{PC}$  is the average percent correct and is the percentage correct of the apples class (the others are similarly defined). The average percent correct weighs each class equally.  $PC_{apples}$

Accuracy is similar to average percent correct, except that accuracy weighs classes with more members more heavily in the calculation. The accuracy of the three-class problem is

$$Acc = \frac{(N_{apples} PC_{apples}) + (N_{oranges} PC_{oranges}) + (N_{bananas} PC_{bananas})}{N_{total}} \quad (73)$$

where  $Acc$  is the accuracy, is the number of apples (the others are similarly defined), and is the total number of fruit pieces. A modified confusion matrix including average percent correct and accuracy is shown in Table 13 on the next page.  $N_{apples} N_{total}$

Table 13. Modified three-class confusion matrix.

		Chosen Class			% Error	% Correct
		Apples	Oranges	Bananas		
Actual Class	Apples	6	3	1	40	60
	Oranges	1	12	2	20	80
	Bananas	2	3	15	25	75
				Average	28.3	71.7
				Accuracy	73.3	

The modified confusion matrix will be used throughout the remainder of this report to analyze classification performance.

## Section 10 Classification Performance

### 10.1 Introduction.

This section uses the confusion matrix to quantify and analyze the radar's classification performance. We warn the reader to be cautious in interpreting the classification results of any classifier. The performance of *all* classifiers depends on the amount and type of data collected. Classification results can be skewed by too little data or an abundance of overly simple test cases. Special attention was paid to this issue during the course of this project. An extensive database of radar signatures was collected with widely varying speeds, approach angles, ranges, and postures. We attempted to simulate potential operational conditions as much as possible. However, the radar should be tested in actual operational conditions over a long time period to provide the most accurate estimate of classification performance.

### 10.2 Classifier Performance.

A total of 1,508 frames of data were used to test the performance of the classifier. The classifier testing database contained 1,183 human data frames, 176 vehicle data frames, and 149 animal data frames. The overall performance of the classifier using the entire testing database is shown in Table 14.

Table 14. Three-class confusion matrix of combined database.

		Chosen Class			% Error	% Correct
		Human	Vehicle	Animal		
Actual Class	Human	1113	16	54	5.92	94.08
	Vehicle	34	137	5	22.16	77.84
	Animal	12	0	137	8.05	91.95
				Average	12.04	87.96
				Accuracy	91.98	

The classifier is seen to perform quite well with an overall average percent correct of 87.96% and an accuracy of 91.98%. A good portion of the overall error is introduced from vehicles being misclassified as humans. The vehicle dataset contains several files where the vehicle's aspect angle with respect to the radar is near 90°. These near-perpendicular aspect angles both reduce the received signal power and increase the vehicle target's spectrogram bandwidth. These two influences can cause the classifier to misclassify a vehicle as a human.

In most physical security applications, distinguishing a human target from a vehicular target is unnecessary since both are considered threats. To demonstrate the classifier's performance in physical security applications, humans and vehicles will be grouped as the "threat" class while animals will be considered to be the "non-threat" class. Table 15 shows the results of the threat/non-threat grouping.

Table 15. Two-class confusion matrix of combined database.

		Chosen Class		% Error	% Correct
		Threat	Non-threat		
Actual Class	Threat	1300	59	4.34	95.66
	Non-threat	12	137	8.05	91.95
$P_{fa,class}$	8.05%	Average		6.20	93.81
$P_{d,class}$	95.66%				

The probability of false alarm (for classification) is 8.05%. This means that when an animal is actually present in the radar coverage area, 8.05% of the time (on average) it will be misclassified as either a human or a vehicle. The probability of detection (for classification) is 95.66%. When a human or vehicle is actually present in the radar coverage area, 95.66% of the time (on average) it will be correctly classified as either a human or a vehicle.

It is important to split the complete testing database into smaller subsets to investigate if the classifier has weaknesses against a particular target type or target maneuver. To further investigate the probability of false alarm for detection, the animal class was split into goat, dog, and deer subsets. Tables 16, 17, and 18 display the classifier's performance against each individual animal grouping. The results show that the classifier performed best on the dog subset. Of the three animal types tested, the deer subset was the most difficult for the classifier.

Table 16. Two-class confusion matrix with only goats in the animal class.

		Chosen Class			
		Threat	Non-threat	% Error	% Correct
Actual Class	Threat	1300	59	4.34	95.66
	Non-threat	8	87	8.42	91.58
$P_{fa,class}$	8.42%	Average		6.38	93.62
$P_{d,class}$	95.66%				

Table 17. Two-class confusion matrix with only dogs in the animal class.

		Chosen Class			
		Threat	Non-threat	% Error	% Correct
Actual Class	Threat	1300	59	4.34	95.66
	Non-threat	1	29	3.33	96.67
$P_{fa,class}$	3.33%	Average		3.84	96.17
$P_{d,class}$	95.66%				

Table 18. Two-class confusion matrix with only deer in the animal class.

		Chosen Class			
		Threat	Non-threat	% Error	% Correct
Actual Class	Threat	1300	59	4.34	95.66
	Non-threat	3	21	12.50	87.50
$P_{fa,class}$	12.50%	Average		8.42	91.58
$P_{d,class}$	95.66%				

The ability to detect and correctly classify crawling humans is of vital importance to physical security applications. The human dataset was split into a subset of crawling and non-crawling data to evaluate the classifier's performance against crawlers. Table 19 and Table 20 shows the three-class and two-class confusion matrices of the crawler data, respectively.

Table 19. Three-class confusion matrix with only crawlers in the human class.

		Chosen Class				
		Human	Vehicle	Animal	% Error	% Correct
Actual Class	Human	337	3	20	6.39	93.61
	Vehicle	34	137	5	22.16	77.84
	Animal	12	0	137	8.05	91.95
				Average	12.20	87.80
				Accuracy	89.20	

Table 20. Two-class confusion matrix with only crawlers in the human subset.

		Chosen Class			
		Threat	Non-threat	% Error	% Correct
Actual Class	Threat	511	25	4.66	95.34
	Non-threat	12	137	8.05	91.95
$P_{fa,class}$	8.05%	Average		6.36	93.65
$P_{d,class}$	95.34%				

The classifier is seen to perform quite well on crawling human targets. The good performance against crawlers is largely due to the legswing period feature. Even fast-moving crawlers produce long limb motion periods relative to most animal targets of interest.

The current target tracking algorithm does not simultaneously track multiple targets. This issue naturally raises concerns about classifier performance when multiple targets are present. To evaluate classification performance under multiple target scenarios, the human and vehicle data was split into multiple target and single target subsets. A classification was judged as correct if the target of highest received signal power was classified correctly. Tables 21 and 22 show the three-class and two-class confusion matrices of the multiple-target subset, respectively.

Table 21. Three-class confusion matrix with only multiple-target files in the human and vehicle classes.

		Chosen Class				
		Human	Vehicle	Animal	% Error	% Correct
Actual Class	Human	278	3	14	5.76	94.24
	Vehicle	4	43	1	10.42	89.58
	Animal	12	0	137	8.05	91.95
				Average	8.08	91.92
				Accuracy	93.09	

Table 22. Two-class confusion matrix with only multiple-target files in the threat class.

		Chosen Class			
		Threat	Non-threat	% Error	% Correct
Actual Class	Threat	328	15	4.3766	95.63
	Non-threat	12	137	8.05	91.95
$P_{fa,class}$	8.05%	Average		6.21	93.79
$P_{d,class}$	95.63%				

The classifier is seen to perform well even with multiple targets present. Potential future improvements to the classifier will include simultaneous multiple target classification.

## **Section 11**

### **Conclusion**

#### **11.1 Accomplishments and Future Work.**

This project achieved its main objectives to design hardware, develop target detection and classification algorithms, and collect an extensive radar signature database. Most of the radar design requirements were met or exceeded including range accuracy, maximum unambiguous range, azimuth angular coverage, and per-unit cost. The radar achieved the maximum detectable range requirement for human and vehicle targets. However, small radar cross section animal subjects did not meet this requirement. Joint time-frequency detection and ranging algorithms were successfully designed. In addition, a diverse micro-Doppler signature database was collected and analyzed. The classifier was shown to perform well on an extensive radar signature database.

Although the results of this research are encouraging, more work can be done. One of the main issues to be addressed is detection in widely varying noise environments. Specifically, we plan to investigate the use of Constant False Alarm Rate (CFAR) detectors to improve detection performance in varying weather conditions such as heavy rain or snow. We intend to further improve overall classification performance and design algorithms to simultaneously track and classify multiple targets. Another future goal is to find better methods of analyzing system performance. Finally, we intend to expand the current radar signature database.

## Section 12

### References

- [1] J. Pitton, L. Atles, and P. Loughlin, "Applications of positive time-frequency distributions to speech processing," *IEEE Transactions on Speech and Audio Processing*, vol. 2, No. 4, p. 555, Oct. 1994.
- [2] V. Chen and H. Ling, *Time-Frequency Transforms for Radar Imaging and Signal Analysis*, Norwood, MA: Artech House, 2002.
- [3] J.L. Geisheimer, W.S. Marshall, and E.F. Greneker, "A high-resolution Doppler model of human gait," *Proceedings of SPIE, Vol. 4744 Radar Sensor Technology and Data Visualization*, April 2002.
- [4] M. Solano, J. Ipiná, J. Zamanillo, and C. Pérez-Vega, "X-band Gunn diode oscillator for a multiple-frequency continuous-wave radar for educational purposes," *IEEE Transactions on Speech Education*, vol. 45, No. 4, p. 317, Nov. 2002.
- [5] M. Skolnik, *Introduction to Radar Systems*, New York, NY: McGraw-Hill, pp. 106-111, 1962.
- [6] S.O. Rice, "Mathematical analysis of random noise," *Bell System Tech. J.* vol. 24, pp. 46-156, 1945.
- [7] G. Brooker, "Detection of signals in noise,"  
  
<http://www.acfr.usyd.edu.au/teaching/4th-year/mech4721-signals/material/lecture%20notes/index.html>.
- [8] X.G. Xia, "A quantitative analysis of SNR in the short-time Fourier transform domain for multicomponent signals," *IEEE Trans. on Signal Processing*, Vol. 46, No. 1, pp. 200-203, 1998.
- [9] X.G. Xia, G.Y. Wang, and V.C. Chen, "A quantitative signal-to-noise ratio analysis for ISAR imaging using joint time-frequency analysis – short time Fourier transform," *IEEE Trans. on Aerospace and Electronic Systems*, 2000.
- [10] W. Press, S. Teukolsky, W. Vetterling, and B. Flannery, *Numerical Recipes in C, The Art of Scientific Computing: Second Edition*, Cambridge University Press, pp. 226-229, 1992.

- [11] O. Marichev and M. Trott, "Inversebetaregularized," April 2005,  
<http://functions.wolfram.com/GammaBetaErf/InverseBetaRegularized/>.
- [12] M. Frerking, *Digital Signal Processing in Communication Systems*, New York, NY: Van Nostrand Reinhold, pp. 73-77, 1994.
- [13] D.R. Wehner, *High-Resolution Radar: Second Edition*, Norwood, MA: Artech House, 1995.
- [14] S.L. Marple, Jr., "Large dynamic range time-frequency signal analysis with application to helicopter Doppler radar data," *Signal Processing and its Applications, Sixth International, Symposium on*, Vol.1, pp. 260-263, 2001.

## Appendix A

### Glossary of Terms

*Autocovariance Function* – a signal processing tool that calculates the similarity of a signal to a time-delayed copy of itself. The autocovariance function can be used to quantify a signal's periodicity.

*Average System False Alarm Time* – the average time between system-level false alarms which sets the probability of false alarm.

*Confusion Matrix* – a method of quantifying classifier performance which lists the decisions made by the classifier.

*Constant False Alarm Rate (CFAR) Detector* – a detection method that varies the threshold level in order to maintain a constant false alarm rate under different noise conditions. The noise level is repeatedly estimated and used to vary the threshold.

*dBm* – a unit of measuring power which translates to “dB relative to one milliwatt.” Power in dBm is related to power in watts by:  $Power(in\ dBm) = 10 \log_{10} \left( \frac{Power(in\ watts)}{1\ mW} \right)$ .

*Discrete Fourier Transform (DFT)* – a linear transformation that transforms a signal in the time domain into the frequency domain. The DFT is a widely used signal processing tool often applied to frequency analysis of stationary signals.

*Doppler Frequency* – the difference between transmitted and received signal frequencies which is proportional to a target's velocity relative to the observer.

*Fast Fourier Transform (FFT)* – a computationally fast implementation of the Discrete Fourier transform (DFT). If  $N$  is the length of the transform, the DFT is of order  $N^2$  while the FFT is of order  $N \log N$ . If  $N$  is the length of the transform, the DFT is of order  $N^2$  while the FFT is of order  $N \log N$ .

*Feature Extraction* – the process of quantifying target features for potential use in classification algorithms.

*Feature Space* – a multi-dimensional structure which offers a geometrical view of classification.

*Feature Vector* – a vector of classification features which maps each data frame into a single point in feature space.

*Inphase/Quadrature (I/Q) Channels* – two channels within a receiver that ideally are equal amplitude and  $90^\circ$  out of phase. I/Q channels are required to preserve the direction of target motion in a direct-conversion receiver.

*Joint Time-Frequency (JTF)* – signal processing techniques which analyze the time-varying frequency content of a signal.

*Maximum Target Range* – the estimated maximum range at which a target of a specified radar cross section is detectable, given a required probability of detection and false alarm.

*Maximum Unambiguous Range* – the maximum range to any target when the range calculation becomes ambiguous.

*Micro-Doppler* – Doppler frequency returns produced by target features that do not move at the same velocity as the bulk target. Micro-Doppler can be used to assist target detection and classification.

*Multipath* – distortion that occurs when a transmitted signal reaches a receiver from multiple propagation paths (often the result of reflections off of the ground or a building). The multiple received signals interfere (due to differing signal phase) which distorts the transmitted signal.

*Multiple Frequency Continuous Wave (MFCW) Radar* – a radar that provides both target range and Doppler frequency (velocity) information by simultaneously transmitting a (finite) set of tones.

*Neyman-Pearson Detector* – a detection criterion which fixes the probability of false alarm while maximizing the probability of detection (subject to a constant threshold).

*Noise Figure* – refers to the reduction of signal to noise ratio from the input to the output of a device.

*Point Scatterer Model* – a target model extensively used in radar signal analysis that represents a target as a compilation of a discrete number of scattering points.

*Probability of Detection* – the probability that a detector correctly decides that a signal in noise is present when a signal in noise is actually present.

*Probability of False Alarm* – the probability that a detector incorrectly decides that a signal in noise is present when only noise is actually present.

*Radar Cross Section (RCS)* – (roughly) the ratio of scattered power (per unit solid angle) to incident power density.

*Range Accuracy* – the root mean square (rms) error in calculating the range to a target.

*Short Time Fourier Transform (STFT)* – a linear transformation that transforms a signal in the time domain into the time-frequency domain. The STFT is useful for target detection, ranging, and classification of non-stationary (non time-varying statistics) signals.

*Signal to Noise Ratio (SNR)* – the ratio of average signal power to average noise power. The SNR is often expressed in decibel form. average signal power to av

*Spectrogram* – the magnitude-squared of the short time Fourier transform

*Time-Frequency-Range Diagram (TFR gram)* – a representation of MFCW radar signals that displays the range to a target versus time and frequency.

*Testing Database* – a set of data files used to test a classifier.

*Training Database* – a set of data files used to train a classifier.

## DISTRIBUTION LIST

### DEPARTMENT OF DEFENSE

DEFENSE THREAT REDUCTION AGENCY  
8725 JOHN J. KINGMAN ROAD, MS-6201  
FORT BELVOIR, VA 22060-6201  
ATTN: CSNS  
ATTN: CSA

DEFENSE THREAT REDUCTION AGENCY  
8725 JOHN J. KINGMAN ROAD, SUITE 0944  
FORT BELVOIR, VA 22060-6218  
ATTN: DTIC/OCA

DEFENSE THREAT REDUCTION AGENCY  
ALBUQUERQUE OPERATIONS  
1680 TEXAS STREET, SE  
KIRTLAND AFB, NM 87117-5669  
ATTN: DTRIAC

ASSISTANT TO THE SECRETARY OF DEFENSE  
NUCLEAR, CHEMICAL AND  
DEFENSE PROGRAMS  
THE PENTAGON, ROOM 3C125  
WASHINGTON, DC 20301  
ATTN: DEPUTY FOR NUCLEAR MATTERS

JOINT CHIEFS OF STAFF  
DIRECTOR OF OPERATIONS, J-3  
THE PENTAGON  
3000 DEFENSE, ROOM 2E230  
WASHINGTON, DC 20318-3000  
ATTN: J-34

OFFICE OF SPECIAL TECHNOLOGY  
TECHNICAL SUPPORT WORKING GROUP  
CRYSTAL GATEWAY NORTH  
1111 JEFFERSON DAVIS HIGHWAY, SUITE 116  
ARLINGTON, VA 22212  
ATTN: G. D. SMITH

U.S. NUCLEAR COMMAND AND CONTROL  
SYSTEMS SUPPORT STAFF (NSS)  
SKYLINE 3  
5201 LEESBURG PIKE, SUITE 500  
FALLS CHURCH, VA 22041-3202  
ATTN: SECURITY PROGRAM MANAGER

HQ EUCOM, J-4  
UNIT 30400, BOX 1000  
APO AE 09128  
ATTN: ECJ4-LW

### DEPARTMENT OF THE ARMY

PRODUCT MANAGER  
FORCE PROTECTION SYSTEMS  
5900 PUTNAM ROAD, SUITE 1  
FORT BELVOIR, VA 22060-5420  
ATTN: PRODUCT MANAGER

DEPARTMENT OF THE ARMY  
OFFICE OF THE PROVOST MARSHAL  
THE PENTAGON, 2800 ARMY  
WASHINGTON, DC 20310-2800  
ATTN: DAMP-MPD-PS

US ARMY NUCLEAR & CHEMICAL AGENCY  
7150 HELLER LOOP, SUITE 101  
SPRINGFIELD, VA 22150-3198  
ATTN: MONA-SU

ENGINEER RESEARCH AND  
DEVELOPMENT CENTER  
WATERWAYS EXPERIMENT STATION  
3909 HALLS FERRY ROAD  
VICKSBURG, MS 39180-6199  
ATTN: CEERD-GS-M

### DEPARTMENT OF THE NAVY

OPNAV  
N3N5 - NCIS  
THE PENTAGON, ROOM 1D652  
WASHINGTON, DC 20350-2000  
ATTN: A. N. DUONG

NAVAL FACILITIES ENGINEERING  
SERVICE CENTER  
1000, 23<sup>RD</sup> AVENUE  
PORT HUENEME, CA 93043-4370  
ATTN: CODE ESC-66

STRATEGIC SYSTEMS PROGRAMS  
2521 CLARK STREET, SUITE 1000  
ARLINGTON, VA 22202-3930  
ATTN: SP11

U.S. MARINE CORPS  
THE PENTAGON, ROOM 4A324  
WASHINGTON, DC 20374-1775  
ATTN: J. CAIN

SPACE AND NAVAL WARFARE  
SYSTEMS CENTER  
53560 HULL STREET  
SAN DIEGO, CA 92152-5000  
ATTN: E. BAXTER

#### **DEPARTMENT OF THE AIR FORCE**

UNITED STATES AIR FORCE  
DEPUTY FOR FORCE PROTECTION, AF XOS-F  
1777 NORTH KENT STREET, SUITE 4400  
ROSSLYN, VA 22209  
ATTN: SPO  
ATTN: SPX

U.S. AIR FORCES EUROPE  
APO AE 09094-5001  
ATTN: USAFE/SPO  
ATTN: USAFE/SPX

CHIEF ADVANCED TECHNOLOGY FLIGHT  
642<sup>ND</sup> ELECTRONIC SYSTEMS SQUADRON  
45 ARNOLD STREET  
BUILDING 1600, ROOM 121-M  
HANSCOM AFB, MA 01731-2816  
ATTN: 642<sup>ND</sup> ELSS/FPT

U. S. AIR FORCE  
SECURITY FORCES CENTER  
1517 BILLY MITCHELL BOULEVARD,  
BUILDING 954  
LACKLAND AFB, TX 76236-5228  
ATTN: SPO  
ATTN: SPX

#### **DEPARTMENT OF ENERGY**

DEPARTMENT OF ENERGY  
GERMANTOWN BUILDING  
1100 INDEPENDENCE AVENUE, SW  
WASHINGTON, DC 20585-1290  
ATTN: SO-13

#### **OTHER GOVERNMENT**

NATIONAL ARCHIVES & RECORDS  
ADMINISTRATION  
8601 ADELPHI ROAD, ROOM 3360  
COLLEGE PARK, MD 20740-6001  
ATTN: USER SERVICE BRANCH

#### **DEPARTMENT OF DEFENSE CONTRACTORS**

COMPUTER SCIENCES CORPORATION  
7405 ALBAN STATION COURT, SUITE B-200  
SPRINGFIELD, VA 22150  
ATTN: B. BRLETICH